

## THE LONG-TERM VARIABILITY OF THE X-RAY SOURCES IN NGC 6946 AND NGC 4485/4490

JOEL K. FRIDRIKSSON<sup>1,2</sup>, JEROEN HOMAN<sup>2</sup>, WALTER H. G. LEWIN<sup>1,2</sup>, ALBERT K. H. KONG<sup>3</sup>, AND DAVID POOLEY<sup>4</sup>  
*ApJS, in press*

### ABSTRACT

We analyze data from five *Chandra* observations of the spiral galaxy NGC 6946 and from three *Chandra* observations of the irregular/spiral interacting galaxy pair NGC 4485/4490, with an emphasis on investigating the long-term variability exhibited by the source populations. We detect 90 point sources coincident with NGC 6946 down to luminosities of a few times  $10^{36}$  ergs  $s^{-1}$ , and 38 sources coincident with NGC 4485/90 down to a luminosity of  $\sim 1 \times 10^{37}$  ergs  $s^{-1}$ . Twenty-five (15) sources in NGC 6946 (NGC 4485/90) exhibit long-term (i.e., weeks to years) variability in luminosity; 11 (4) are transient candidates. The single ultraluminous X-ray source (ULX) in NGC 6946 and all but one of the eight ULXs in NGC 4485/90 exhibit long-term flux variability. Two of the ULXs in NGC 4485/90 have not been identified before as ultraluminous sources. The widespread variability in both systems is indicative of the populations being dominated by X-ray binaries, and this is supported by the X-ray colors of the sources. The distribution of colors among the sources indicates a large fraction of high-mass X-ray binaries in both systems. The shapes of the X-ray luminosity functions of the galaxies do not change significantly between observations and can be described by power laws with cumulative slopes  $\sim 0.6 - 0.7$  (NGC 6946) and  $\sim 0.4$  (NGC 4485/90).

*Subject headings:* galaxies: individual (NGC 6946, NGC 4485, NGC 4490) — X-rays: binaries — X-rays: galaxies

### 1. INTRODUCTION

The systematic study of X-ray source populations in external galaxies first became possible with the *Einstein* Observatory in 1978. Significant advances in the field were made with subsequent satellites such as *ROSAT*, but a giant leap forward has been taken with *Chandra*. With its subarcsecond spatial resolution and high sensitivity it is possible to resolve the vast majority of the luminous ( $\gtrsim 10^{37}$  ergs  $s^{-1}$ ) X-ray sources in galaxies out to distances of 20 – 30 Mpc. In addition, the spectrometric capabilities of the *Chandra* ACIS CCD detector allow spectral properties of sources to be extracted. For two recent reviews of the study of X-ray sources in normal galaxies, emphasizing results from *Chandra*, see Fabbiano & White (2006) and Fabbiano (2006).

We now know that X-ray source populations in galaxies are dominated at high luminosities ( $\gtrsim 10^{37}$  ergs  $s^{-1}$ , the range typically explored with *Chandra* observations) by X-ray binaries (XRBs) consisting of an accreting neutron star or black hole and a stellar companion. In addition, galaxies usually have a few young supernova remnants (SNRs) in this luminosity range. Unsurprisingly, the X-ray populations in early-type galaxies (E and S0) seem to consist mostly of low-mass X-ray binaries (LMXBs), whereas galaxies with younger stellar populations (spiral and irregular galaxies) typically have a much higher fraction of the shorter lived high-mass X-ray binaries (HMXBs). In galaxies with a high star formation rate

HMXBs are especially common.

An important class of sources in external galaxies are the so-called ultraluminous X-ray sources (ULXs), usually defined as non-nuclear sources with implied isotropic X-ray luminosities  $\geq 10^{39}$  ergs  $s^{-1}$ . Detections of ULXs with luminosities as high as  $\sim 10^{41}$  ergs  $s^{-1}$  have been reported (see, e.g., Davis & Mushotzky 2004). The nature of ULXs is still debated, and it has been argued that at least some of them might be a new class of objects, so-called intermediate-mass black holes (IMBHs) with masses  $M \sim 10^2 - 10^4 M_{\odot}$  (see, e.g., Miller & Colbert 2004).

We present in this paper the X-ray source population study of the spiral galaxy NGC 6946 and the interacting irregular/spiral system NGC 4485/4490. A special emphasis is placed on studying the long-term (weeks to years) variability properties of the source populations. These galaxies were chosen because they are nearby ( $D \lesssim 8$  Mpc) and have multiple (three or more) long ( $\gtrsim 20$  ks) *Chandra* ACIS exposures spanning a baseline of a few years. Both show an enhanced star formation rate. The spiral NGC 6946 also has the fortunate characteristic of being observed nearly face-on, and the NGC 4485/90 system has low Galactic extinction and a large number of ULXs. For more background information on the galaxies, see §§ 3.1 and 3.2.

Not much work has been done on the long-term variability of X-ray sources in external galaxies, since *Chandra* observations at multiple epochs are usually not available. We know from observations in our own Galaxy that time variability of various kinds, including transient outbursts, eclipses, dips, as well as less severe variations in flux, is very common among XRBs. Temporal and spectral analysis carried out for the most luminous sources in nearby galaxies shows behavior similar to that in Galactic XRBs, clearly pointing to XRB populations

<sup>1</sup> Department of Physics, Massachusetts Institute of Technology, Cambridge, MA 02139; joelkf@mit.edu.

<sup>2</sup> MIT Kavli Institute for Astrophysics and Space Research, Cambridge, MA 02139.

<sup>3</sup> Institute of Astronomy and Department of Physics, National Tsing Hua University, Hsinchu, Taiwan 30013.

<sup>4</sup> Department of Astronomy, University of Wisconsin–Madison, Madison, WI 53706.

(see Fabbiano 2006, and references therein). For example, Kong et al. (2002) find that among 204 detected sources in M31, 50% are variable on timescales of months and 13 are transients. Sivakoff et al. (2005b) find short-timescale flares in 3 out of 157 sources in the elliptical galaxy NGC 4697, and two of the flares have durations and luminosities similar to Galactic superbursts (thermonuclear bursts with very long (hours) durations and very large fluences; see Kuulkers 2004). Sivakoff et al. (2005a) also find long-term variability in 26 out of 124 sources in NGC 4697, and 11 of those are transient candidates. Zezas et al. (2006), analyzing seven *Chandra* observations of the Antennae galaxies, find intensity and/or spectral variability among sources on timescales of years, months, days, and hours. Overall,  $\sim 50\%$  of the sources detected in each observation show either spectral or intensity variation but do not all follow a common trend, indicating that there are various classes of sources. Of the 14 ULXs in the Antennae, 12 show long-term variability. In general, variability of some sort is very common among ULXs (see Fabbiano & White 2006; Fabbiano 2006). Despite widespread variability in luminosity among individual sources, X-ray luminosity functions (XLFs) seem to be remarkably stable from one observation to another, as indicated by observations of NGC 5128 (Kraft et al. 2001), M33 (Grimm et al. 2005), and the Antennae (Zezas et al. 2007).

The organization of the paper is as follows. In § 2 we describe the common analysis steps performed for both galaxies, including source detection, photometry, the construction of light curves and hardness ratios, and testing for flux and spectral variability. In § 3 we discuss general properties and the observations of the galaxies and present the results of the source detection. In § 4 we present and discuss our results on various properties of the source populations in the galaxies. Finally, in § 5 we briefly summarize our results. Included are tables with the source catalog for each galaxy and various observed and derived parameters for each source.

## 2. DATA ANALYSIS

The *Chandra* observations of both galaxies were analyzed with the CIAO software, version 3.4 (CALDB ver. 3.3.0), and with ACIS Extract (hereafter AE), version 3.131. AE is an ACIS point source extraction package developed at Pennsylvania State University (Broos et al. 2002), which assists in a large variety of complex data processing tasks. The procedures used in AE are described in Townsley et al. (2003) and Getman et al. (2005). We note that all errors mentioned in this paper are, unless explicitly stated otherwise, Poisson errors with a confidence level corresponding to  $1\sigma$  Gaussian. They were computed using the Gehrels approximation of Poisson limits (Gehrels 1986).

### 2.1. Source detection

The level 1 event files from the *Chandra* data archive were reprocessed, and new level 2 event files created by following the standard ACIS data preparation procedure recommended by the *Chandra* X-ray Center (CXC).<sup>5</sup> The data were checked for periods of unusually high background. No such periods were found in any observation

of either galaxy. A monochromatic exposure map evaluated at 1.5 keV was created for each observation, and the event files, as well as the exposure maps, merged to create a co-added exposure covering all the observations. A 0.3–7 keV band image encompassing the whole galaxy was subsequently created from the merged event file, and `wavdetect`, the CIAO wavelet source detection algorithm, run at nine scales (1,  $\sqrt{2}$ , 2,  $2\sqrt{2}$ , 4,  $4\sqrt{2}$ , 8,  $8\sqrt{2}$ , and 16 pixels), using the merged exposure map (the `sigthresh` parameter, which sets the threshold for identifying a pixel as belonging to a source, was set at a value of 1 over the number of pixels in the image<sup>6</sup>).

Further analysis was performed with AE. The input to the program was the master source list from the `wavdetect` run and the cleaned event data for each observation. After visual inspection of the data (both co-added and individual exposures) a few extra candidate sources, not detected by `wavdetect`, were typically added to the list. Since we only perform source detection on the co-added exposure, it is conceivable that `wavdetect` might for example miss weak transient sources in high-background regions. In the end, only in one case did such a candidate source end up surviving the significance cuts described below. Source CXOU J123038.2+413831 in NGC 4485/90 is in close proximity to a much brighter transient source, causing `wavdetect` to detect only the brighter source in the co-added exposure. The existence of two individual sources is readily apparent when looking at individual observations, in some of which the brighter source is in quiescence.

An important characteristic of AE is that it tailors the count extraction region individually to each source in each observation based on the shape of the point spread function (PSF) at the source location on the detector. Counts were by default extracted from a region with a PSF encircled energy fraction of 0.90, but in cases of crowded sources AE automatically reduces the fraction to prevent overlapping extraction regions. The response functions computed by AE are corrected to take into account the flux missed by the finite extraction region in each case.

Possibly spurious detections from our candidate source list were rejected based on a source significance statistic computed by AE (for definition see Broos et al. 2002), along with visual inspection of the individual and merged observations, as well as the `wavdetect` significance statistic.<sup>7</sup> We set a conservative limit where detections with AE significance  $\lesssim 3 - 3.5\sigma$  (which typically corresponds to `wavdetect` significance  $\lesssim 5 - 6\sigma$  for the co-added exposure) were rejected.

The source positions were overlaid on an optical image of the galaxy along with the  $D_{25}$  elliptical isophote (obtained from de Vaucouleurs et al. 1991). In general, we considered sources inside the  $D_{25}$  isophote to be coincident with the system and removed other sources from the list. However, in a few cases sources just outside the isophote were included based on visual inspection of the galaxy’s optical extent, which can be quite irregular. The accuracy of the source positions was refined

<sup>6</sup> See <http://cxc.harvard.edu/ciao/ahelp/wavdetect.html>.

<sup>7</sup> See definition in The *Detect Reference Manual*, available online at [http://cxc.harvard.edu/ciao/download/doc/detect\\_manual/index.html](http://cxc.harvard.edu/ciao/download/doc/detect_manual/index.html).

<sup>5</sup> See [http://cxc.harvard.edu/ciao/guides/acis\\_data.html](http://cxc.harvard.edu/ciao/guides/acis_data.html).

with the help of AE. Since the average off-axis angle was  $\lesssim 5'$  for nearly all sources, we used positions based on the centroid of the extraction regions as recommended in Broos et al. (2002).

### 2.2. Light Curves

AE is capable of performing extensive broadband photometry. For all sources an estimate of both the photon flux and the energy flux in the 0.3–7 keV band was computed from the AE results for each observation, as well as for the co-added exposure. For all but the faintest sources the photon flux was computed by dividing the number of net (i.e., background-subtracted) counts by the exposure time and the mean effective area at the source location for a given energy band (the MEAN\_ARF parameter in AE, which takes into account flux missed by the finite extraction region). For computing the mean effective area the simplifying assumption of a flat incident spectrum within the given energy band was made. For an estimate of the energy flux the photon flux was multiplied by the mean observed photon energy in the corresponding band, as computed by AE. This was done in five adjacent energy bands spanning together the full 0.3–7 keV band (0.3–1, 1–1.5, 1.5–2.5, 2.5–4, and 4–7 keV), and the results from the individual bands then added together. This is a compromise between calculating the fluxes directly for the full band (and thus assuming a flat incident spectrum over that whole band, which gives rise to a systematic error) and dividing the counts in each spectral channel by the corresponding value of the auxiliary response function (ARF), this latter method being susceptible to large Poisson errors. For the ULXs in the galaxies we performed spectral fitting (see below) and compared the flux results from our “band method” to the spectral fitting results. We found that the values from the band method were typically 5%–10% higher than the ones from spectral fitting and that the discrepancy was usually slightly greater for the photon flux than the energy flux.

For observations of sources with very few counts it is perhaps more sensible to give an upper limit to the flux instead of an actual flux estimate. Since we do not perform source detection on individual observations, only on the co-added exposure, it is effectively meaningless for us to talk about whether a source was detected or not in an observation. We therefore adopt a fixed threshold of five net counts, below which we give upper limits in our tables, with  $3\sigma$  Gaussian confidence, instead of flux values. We calculate the limits with the Sherpa package in CIAO. They are derived from the full-band counts, assuming a power-law spectrum with a photon index of 1.7 (characteristic of best-fit spectra for sources in our sample) and Galactic absorption, and using the response functions at the source location. We note that for the purpose of computing the flux variability parameter described in § 2.4 below, we always use actual flux estimates, although for less than 5 net counts those estimates are calculated using Sherpa (as described above) rather than our band method.

In the case of the ULXs the flux estimates were improved on by fitting eight simple spectral models to each of the *Chandra* observations in XSPEC, and using in each case the best-fitting model to derive the fluxes. The models considered were absorbed power-law, bremsstrahlung,

TABLE 1  
*Chandra* OBSERVATIONS OF NGC 6946

Start Date	Instrument	Obs. ID	Exp. <sup>a</sup> (ks)	Data Mode <sup>b</sup>
2001 Sep 7	ACIS-S	1043	58.29	F
2002 Nov 25	ACIS-S	4404	29.92	F
2004 Oct 22	ACIS-S	4631	29.70	F
2004 Nov 6	ACIS-S	4632	27.94	F
2004 Dec 3	ACIS-S	4633	26.62	F

<sup>a</sup> Good live exposure time.

<sup>b</sup> Telemetry formats: F = Faint.

blackbody, and multicolor disk blackbody models, as well as two-component models with one of the previous components plus an additional power-law component (both equally absorbed). The absorption parameter was allowed to vary freely with a minimum value equal to the Galactic absorption column.

After converting the energy fluxes to luminosities based on our adopted distance to each galaxy long-term light curves (spanning all observations) were created for each source. It should be noted that all fluxes and luminosities quoted in this paper are absorbed values (i.e., they are not corrected for absorption along the line of sight), and they are, unless otherwise noted, given for the 0.3–7 keV range. The error bars shown in light curves and other plots only take into account the Poisson errors in the counts.

### 2.3. Hardness ratios

Hardness ratios were chosen as our primary means of investigating the spectral properties of the source populations, since a large portion of the sources had too few counts to be amenable to spectral fitting. Two kinds of hardness ratios were computed for each source in each observation, as well as for the co-added exposure. Our soft color is defined as

$$\text{HR1} = \frac{M - S}{T}, \quad (1)$$

and the hard color as

$$\text{HR2} = \frac{H - M}{T}, \quad (2)$$

where S, M, H, and T are the net counts in the 0.3–1 keV (soft), 1–2 keV (medium), 2–7 keV (hard), and 0.3–7 keV (total) bands, respectively. The counts used to calculate the hardness ratios were in each case divided by the mean value of the effective area over the given energy band at the location of the source. This was done to account for differences in effective areas between different energy bands, and differences due to variations in source locations on the detector. The errors in the hardness ratios were computed using standard error propagation.

Although it is not possible to conclusively classify an individual source based on its hardness ratios alone, it is possible to draw conclusions about bulk trends within a source population, as shown by Prestwich et al. (2003). They propose a classification scheme based on hardness ratios, in which they identify the regions in a color-color diagram where sources of a given type are most likely to fall. We utilize this method to draw conclusions about the source populations (see § 4.3.3). It should be noted

that our hardness ratio definitions differ slightly from the ones used by Prestwich et al. (2003). They use an upper limit of 8 keV to their hard and total bands, in contrast to our using 7 keV. However, for the vast majority of sources only a very small fraction of the counts in the 0.3 – 8 keV band is between 7 and 8 keV, so this should have a negligible effect. They also use a slightly different method to account for variations in effective area. As Prestwich et al. (2003) discuss in their paper, absorption will tend to blur the distinction in a color-color diagram between the different source types. However, this effect should not be very severe for the galaxies studied in this paper; although NGC 6946 suffers from substantial extinction, it is observed face-on, and the absorption column in the direction of NGC 4485/90 is low (see § 3).

#### 2.4. Variability

We compute a significance parameter for long-term flux variability for each source:

$$S_{\text{flux}} = \max_{i,j} \frac{|F_i - F_j|}{\sqrt{\sigma_{F_i}^2 + \sigma_{F_j}^2}}, \quad (3)$$

where  $F_i$  denotes the photon flux of a source in the  $i$ th *Chandra* observation, and  $\sigma_{F_i}$  is the corresponding error. We define a source as variable if  $S_{\text{flux}} > 3$ . We also quantify the variability by computing the ratio  $R = F_{\text{max}}/F_{\text{min}}$ . We consider a source to be a transient candidate if its measured flux is consistent with zero (within  $\sim 1 \sigma$  error) in at least one observation, and if the source is also clearly variable ( $S_{\text{flux}} > 3$ ).

We test for short-term flux variability (within single observations) by performing a one-sided Kolmogorov-Smirnov test for each source in each observation, comparing event times to a uniform count-rate model. We define a source as showing evidence for variability if the significance of the computed K-S statistic is less than  $3 \times 10^{-3}$  (i.e., if the null hypothesis that the count rate is uniform can be rejected at the 99.7% level or more, corresponding to approximately  $3 \sigma$  Gaussian confidence).

To search for long-term spectral variability, we compute significance parameters for the variability in the hardness ratios. They are defined analogously to the flux variability parameter above. Again, we require  $3 \sigma$  confidence to classify a source as variable.

#### 2.5. ROSAT and XMM-Newton Data

Apart from *Chandra*, there are three other X-ray telescopes that have had good enough spatial resolution to possibly be of significant value to this study. The *Einstein* HRI, the *ROSAT* HRI, and the *XMM-Newton* EPIC cameras all had or have an on-axis resolution of  $\lesssim 10''$ . However, the *Einstein* and *ROSAT* HRIs were only sensitive in the 0.15 – 3.5 and 0.1 – 2.4 keV bands and had negligible energy resolution. None of the galaxies analyzed in this paper was observed with the *Einstein* HRI.

For the ULXs that were well resolved from neighboring bright sources the long-term light curves were extended by adding data points from *ROSAT* and *XMM-Newton* observations. It was usually necessary to use small extraction regions to minimize the contamination from nearby sources and from the diffuse emission in which many sources are embedded.

TABLE 2  
*ROSAT* HRI OBSERVATIONS OF NGC 6946

Start Date	Seq. ID	Exp. <sup>a</sup> (ks)
1994 May 14	rh600501n00	59.89
1995 Aug 13	rh600718n00	21.51
1996 Aug 10	rh500476n00	8.36

<sup>a</sup> Good live exposure time.

#### 2.5.1. ROSAT

*ROSAT* count rates were derived from the RDF (rationalized data format) files available from the *ROSAT* Archive. The event data files were corrected for the HRI aspect error (see, e.g., David et al. 1999) using the correction script developed at the Smithsonian Astrophysical Observatory (SAO).<sup>8</sup> Background-subtracted count rates were extracted using the ASTERIX software package (ver. 2.3-b2). The `xrtsort`, `xrtsub`, and `xrtcorr` tasks were used, which automatically make dead-time, vignetting, and quantum efficiency corrections. In all cases counts were extracted from a circle of radius  $8''$ . For point sources with an off-axis angle  $\lesssim 5'$  the PSF encircled energy fraction for such a circle is  $\sim 0.84$  (David et al. 1999; Zimmermann et al. 1998). The count rates were therefore divided by this number to correct for the counts missed by the finite extraction region.

To facilitate comparison with the *Chandra* results count rates from *ROSAT* were converted to energy flux in the 0.3 – 7 keV band using PIMMS. To determine the spectral model to use for the conversion the eight models described in § 2.2 were fitted to the source spectrum from the co-added *Chandra* exposure, and the best-fitting model used.

#### 2.5.2. XMM-Newton

For *XMM-Newton* data a new analysis was performed for each of three EPIC detectors using the SAS software, versions 7.0.0 and 7.1.0, and the latest available calibration files at the time of the analysis. Starting with the original data files (ODFs) from the *XMM-Newton* archive, MOS and PN data were reprocessed using the `emproc` and `epproc` tasks. After excluding periods of high background, source spectra were extracted with the `evselect` task. The `eregionanalyse` task was used to center the extraction radius on the centroid of the counts distribution for each source. Counts were extracted from circles with radii in the range  $8''$  to  $15''$  as deemed appropriate in each case. The event selection criteria used for the spectral extraction were `PATTERN = 0 – 12` and `FLAG = #XMMEA_EM` for the MOS instruments, and `PATTERN = 0 – 4` and `FLAG = 0` for the PN, as recommended in the analysis threads from the *XMM-Newton* Science Operations Centre.<sup>9</sup> Response files were created using the `rmfgen` and `arfgen` tasks, incorporating a correction for the flux missed by the finite extraction regions. The spectra were fitted with the eight spectral models described in § 2.2. The spectra for each of the three detectors were fitted simultaneously, allowing only

<sup>8</sup> Available online at <http://hea-www.harvard.edu/rosat/aspfix.html>.

<sup>9</sup> See <http://xmm.vilspa.esa.es/sas/7.1.0/documentation/threads/>.

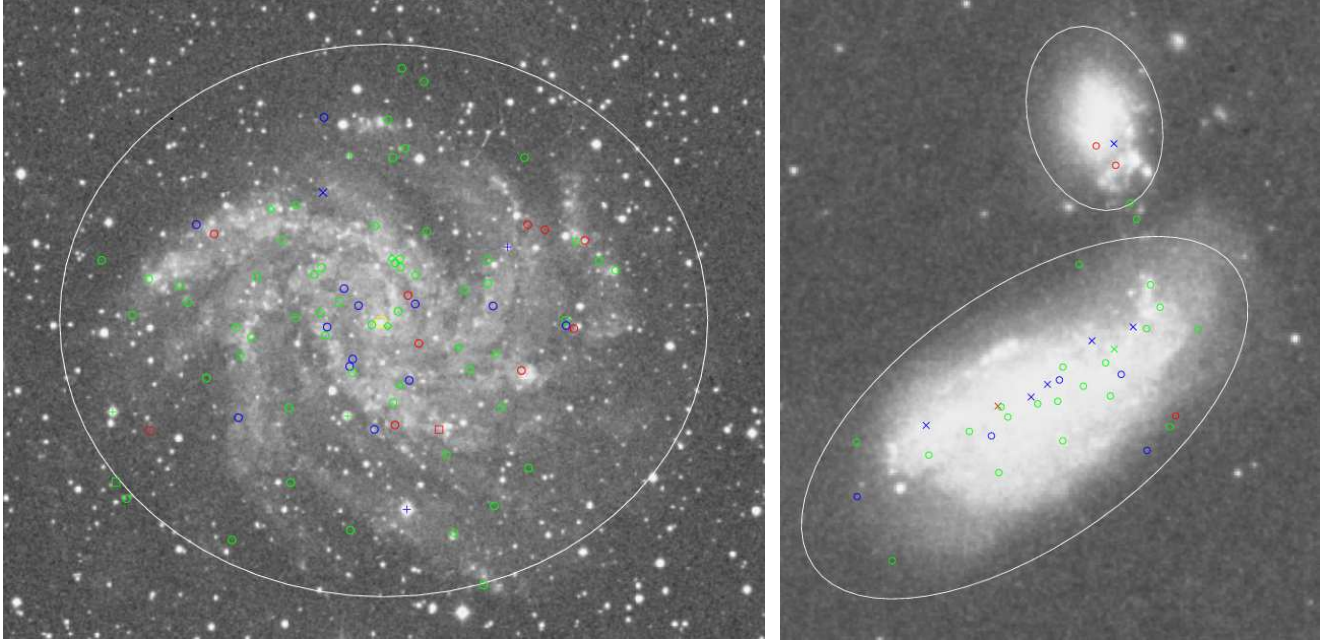


FIG. 1.— DSS images of NGC 6946 (*left*) and NGC 4485/4490 (*right*) with positions of detected X-ray sources overlaid. Foreground stars are represented with plus symbols, historical supernovae with boxes, SNRs with diamonds, ULXs with crosses, and other sources with circles. Blue indicates that long-term variability is detected, green that it is not, and red denotes transient candidates. The white ellipses are the  $D_{25}$  elliptical isophotes and the yellow circle encloses the central area in NGC 6946 that was excluded from analysis.

an overall normalization factor to vary between detectors to account for differences in calibration. Using the best-fitting model for each source, an energy flux in the 0.3 – 7 keV band was then computed. The individual fluxes for the three instruments were combined into a single flux result by taking the mean weighted with the inverse variance (i.e., squared error) of each individual flux.

### 3. OBSERVATIONS AND SOURCE DETECTIONS

#### 3.1. NGC 6946

NGC 6946 is one of the closest large spiral galaxies and is seen nearly face-on. It is classified by de Vaucouleurs et al. (1991) as type SAB(rs)cd. It has been extensively studied in almost all wavelength bands and has been shown to have strong nuclear starburst activity (Elmegreen et al. 1998b). High star formation activity in its disk has also been observed (Sauty et al. 1998), and in agreement with this NGC 6946 has been host to nine recorded supernovae in the last 91 years (three in the past 7 years), currently the highest known number of historical supernovae in any galaxy. The global star formation rate in NGC 6946 for stars in the mass range 2 – 60  $M_{\odot}$  is estimated by Sauty et al. (1998) to be  $\sim 4 M_{\odot} \text{ yr}^{-1}$ , and Crosthwaite & Turner (2007) estimate the dynamical mass of the galaxy to be  $\sim 2 \times 10^{11} M_{\odot}$ .

The distance to NGC 6949 is given by de Vaucouleurs (1979) as 5.1 Mpc and is listed as 5.5 Mpc in Tully (1988), assuming a Hubble constant value of  $75 \text{ km s}^{-1} \text{ Mpc}^{-1}$ . More recently, Eastman et al. (1996) derive a distance of  $5.7 \pm 0.7$  Mpc based on a Type II supernova, and Sharina et al. (1997) find a distance of  $6.4 \pm 0.4$  Mpc based on photometric observations of the brightest stars in the galaxy. Finally, Karachentsev et al. (2000) es-

timate the distance to the NGC 6946 galaxy group (consisting of NGC 6946 and seven other small galaxies) to be  $5.9 \pm 0.4$  Mpc, based on observations of the brightest blue giants in the galaxies. We choose to adopt a distance of 5.9 Mpc, as do Holt et al. (2003), Schlegel et al. (2003), and Larsen et al. (2002). The Galactic absorption column in the direction of NGC 6946 is  $2.0 \times 10^{21} \text{ cm}^{-2}$  (Dickey & Lockman 1990; Stark et al. 1992; Kalberla et al. 2005).

NGC 6946 was first observed in X-rays with the *Einstein* satellite; three observations with the *Einstein* IPC were made in 1979–1981. Analyzing these observations, Fabbiano & Trinchieri (1987) resolve the X-ray emission from the galaxy into two peaks. NGC 6946 was observed with the *ROSAT* PSPC in 1992, twice with the *ASCA* satellite in 1993 and 1994, and three times with the *ROSAT* HRI in 1994–96. Schlegel (1994b) analyzes the *ROSAT* PSPC observation and resolves emission from the galaxy into nine point sources, as well as finding evidence for diffuse emission. Analyzing the first of the three *ROSAT* HRI observations and the second of the two *ASCA* observations Schlegel et al. (2000) detect 14 point sources and diffuse emission from the galaxy. Most recently, NGC 6946 has been observed five times with *Chandra* between 2001 and 2004, and 11 times with *XMM-Newton* in 2003–2006. The most detailed studies so far of the X-ray emission components of NGC 6946 are presented in a pair of papers based on the first of the five *Chandra* observations. Holt et al. (2003) study the point source population and find 72 sources; the diffuse emission is extensively studied in Schlegel et al. (2003).

The *Chandra* observations of NGC 6946 are summarized in Table 1. These are all ACIS-S full-frame imaging observations taken in Timed Exposure mode. The frame time was in all cases set at the standard value of 3.2 s, and events were telemetered in the Faint format.

TABLE 3  
*XMM-Newton* EPIC OBSERVATIONS OF NGC 6946

Start Date	Obs. ID	MOS-1		MOS-2		PN	
		Exp. <sup>a</sup> (ks)	Mode <sup>b</sup> / Filter <sup>c</sup>	Exp. (ks)	Mode/ Filter	Exp. (ks)	Mode/ Filter
2004 Jun 09	0200670101	3.95	FF-ME	4.05	FF-ME	2.50	FF-ME
2004 Jun 13	0200670301	11.47	FF-ME	11.68	FF-ME	8.93	FF-ME
2004 Jun 25	0200670401	7.69	FF-ME	8.49	FF-ME	4.81	FF-ME
2006 Jun 02	0401360201	4.40	FF-ME	4.31	FF-ME	3.81	FF-ME
2006 Jun 18	0401360301	5.28	FF-ME	5.60	FF-ME	3.58	FF-ME

NOTE. — Six additional *XMM-Newton* EPIC observations of NGC 6946 have been made, but those were not used due to high background rates leaving very little good exposure time.

<sup>a</sup> Good live exposure time.

<sup>b</sup> Instrument modes: FF = full frame.

<sup>c</sup> Filters: ME = medium filter.

The observations span a period of about 39 months and have a cumulative good live exposure time of 172.5 ks. In each observation the majority of sources falls on the back-illuminated S3 chip, and a smaller portion falls on the front-illuminated S2 and/or S4 chips. None of the observations covers the whole  $D_{25}$  isophote.

The data were analyzed as described in § 2. Source detection was performed on a  $14.8' \times 14.1'$  rectangle encompassing the system. A circular region of radius  $6''$  at the center of the galaxy (circle centered at R.A. =  $308.71857^\circ$ , decl. =  $60.153726^\circ$ ) was excluded from further analysis, since the sources there are too crowded and embedded in too much localized diffuse emission for reliable background-subtracted count rates to be extracted. This central region seems to contain at least four and possibly six point sources. Outside this region a total of 90 reliable source detections down to luminosities of a few times  $10^{36}$  ergs  $s^{-1}$  (depending on the location) were found to be coincident with the galaxy (see Fig. 1). The source catalog, including selected source parameters, is presented in Table 9. We choose to give photon fluxes for each source in each observation, as opposed to counts or count rates, since the latter two quantities are not directly comparable between different sources and observations due to variations in exposure and effective area.

An adaptively smoothed image based on the co-added *Chandra* exposure is shown in Figure 2. The `csmooth` task in CIAO was used to create smoothed images for the 0.3–1, 1–2, and 2–7 keV bands. The same smoothing scales were used for all three images. The scales were calculated by adaptively smoothing a full-band image with a significance between  $3.5\sigma$  and  $5\sigma$  above the local background. Each of the three images was also exposure corrected using exposure maps smoothed with the same scales as the images. The images were then combined to create a color-coded full-band image with red representing the soft band, green the medium band, and blue the hard band. Finally, to enhance the point sources, the combined image was smoothed with a Gaussian with a kernel radius of three pixels.

Of the 90 sources, 65 were previously detected by Holt et al. (2003) and 25 were not. Holt et al. (2003) also report two sources within the central region excluded from our analysis, as well as one that falls outside the extent of the galaxy as we define it. Moreover, three of their 72 detected sources fall below our significance threshold for inclusion, and, finally, one of their sources almost cer-

tainly suffers from a typographical error in its position (sources 35 and 36 in their Table 1 have the same position to within an ACIS pixel size).

We associate five of our 90 detected sources with foreground stars (see Table 9). Comparing our source locations to the USNO-A2.0 Catalogue (Monet et al. 1998), available online through Vizier, we find that five sources are coincident with foreground stars in the catalog to within  $0.8''$ . We estimate the likelihood of a chance coincidence to be low. For a crude test we shifted the source positions northeast by  $7''$ . This resulted in no matches with sources in the catalog to within  $2.5''$ .

Positions of sources were compared with two existing lists of SNRs in NGC 6946: a list of 27 optically identified SNRs from Matonick & Fesen (1997) and a list of 35 radio-selected SNR candidates from Lacey & Duric (2001). Interestingly, the two lists only have two sources in common. We find one counterpart to a SNR in the former list and five counterparts to SNR candidates in the latter list, as well as a counterpart to one of the two common sources. Two of the nine historical supernovae in the galaxy took place within the timespan covered by the *Chandra* observations, and they are both detected. In addition to these, two of the older historical supernovae are detected.

We estimate how many of our detected sources can be expected to be cosmic background sources (CBSs; primarily active galactic nuclei and star-forming galaxies) by using the results of Bauer et al. (2004) from the *Chandra* Deep Fields. They give formulae estimating the number of CBSs per square degree of the sky above a given limiting flux in two energy bands, 0.5–2 and 2–8 keV. Performing source detection on a merged 0.5–2 keV image from all five observations, 75 of our 85 nonforeground sources were detected with a `wavdetect` significance level above  $5\sigma$ . In the 2–8 keV band, 53 of the 85 sources were detected, five of which were not detected in the soft band. Since the total exposure varies widely over the extent of the galaxy, so does the limiting count rate for detection. For our soft band detections, we estimate that a typical limiting count rate is  $\sim 2 \times 10^{-4}$  counts  $s^{-1}$  in the 0.3–7 keV band, and  $\sim 4 \times 10^{-4}$  counts  $s^{-1}$  for our hard band detections. We convert these count rates to energy fluxes in the soft and hard bands, respectively, assuming a power law with a spectral index of 1.4 (as done by Bauer et al. 2004). We take into account absorption both in our own Galaxy and in NGC 6946. Us-

TABLE 4  
*Chandra* OBSERVATIONS OF NGC 4485/4490

Start Date	Instrument	Obs. ID	Exp. <sup>a</sup> (ks)	Data Mode <sup>b</sup>
2000 Nov 3	ACIS-S	1579	19.52	F
2004 Jul 27	ACIS-S	4725	38.41	VF
2004 Nov 20	ACIS-S	4726	39.59	VF

<sup>a</sup> Good live exposure time.

<sup>b</sup> Telemetry formats: F = Faint, VF = Very Faint.

ing the results of Tacconi & Young (1986), we estimate that a typical absorption column through NGC 6946 is  $\sim 1 \times 10^{21} \text{ cm}^{-2}$ . Adding Galactic absorption, this yields a total absorption column for CBSs of  $\sim 3 \times 10^{21} \text{ cm}^{-2}$ . Using our derived soft and hard band flux limits in the formulae of Bauer et al. (2004), we get 22.4 sources in the soft band over the angular area of the  $D_{25}$  isophote of NGC 6946 (corresponding to 30% of our 75 soft band detections), and 23.6 sources in the hard band, or 45% of our 53 detections. Overall, we estimate that  $\sim 28$  of our total 85 detections in the 0.3 – 7 keV band can be expected to arise from CBSs.

The *ROSAT* HRI and *XMM-Newton* EPIC observations of NGC 6946 are summarized in Tables 2 and 3. A total of 11 *XMM-Newton* EPIC observations have been made, all of which suffer from periods of high background. Six of them are completely unusable and were therefore not analyzed further, and they are not included in Table 3.

### 3.2. NGC 4485/4490

NGC 4485 and NGC 4490 are a closely interacting pair of galaxies, variously classified as spiral or irregular systems (see Fig. 1). In de Vaucouleurs et al. (1991) NGC 4490 is classified as type SB(s)d, and the smaller companion NGC 4485 as type IB(s)m. Both galaxies show signs of tidal disruption. Tully (1988) gives separate distances of 7.8 Mpc (NGC 4490) and 9.3 Mpc (NGC 4485) to the two galaxies, assuming a Hubble constant value of  $75 \text{ km s}^{-1} \text{ Mpc}^{-1}$ . These distances are adopted by Roberts & Warwick (2000) and Liu & Bregman (2005). Such disparate distances are, however, unphysical for such a closely interacting system. Roberts et al. (2002), Elmegreen et al. (1998a), and Read et al. (1997) therefore assume a distance of 7.8 Mpc to both galaxies. A consistent distance of 8 Mpc to the pair is adopted by Clemens & Alexander (2002), Clemens et. al (1998, 1999, 2000), Thronson et al. (1989), and Viallefond et al. (1980), based on the suspected membership of the system in the CVn II cloud (de Vaucouleurs et al. 1976), and this is the value we used. The Galactic absorption column in the direction of NGC 4485/4490 is  $1.8 \times 10^{20} \text{ cm}^{-2}$  (Dickey & Lockman 1990; Stark et al. 1992; Kalberla et al. 2005).

NGC 4485/90 has been studied at radio, infrared, and optical wavelengths and shows evidence for enhanced star formation (Viallefond et al. 1980; Klein 1983; Thronson et al. 1989). Clemens et. al (1999) estimate a star formation rate in NGC 4490 of  $\sim 4.7 M_{\odot} \text{ yr}^{-1}$  and a dynamical mass of  $\sim 1.6 \times 10^{10} M_{\odot}$  within 8 kpc (the companion NGC 4485 being less massive by about a factor of 8). The system was first ob-

TABLE 5  
*ROSAT* HRI OBSERVATIONS OF NGC 4485/4490

Start Date	Seq. ID	Exp. <sup>a</sup> (ks)
1996 Jun 18	rh600855n00	26.70
1996 Nov 26	rh600855a01	24.58

NOTE. — One additional *ROSAT* HRI observation was made. We did not make use of it due to its shortness.

<sup>a</sup> Good live exposure time.

served in X-rays with the *ROSAT* PSPC in 1991. Analyzing those data, Read et al. (1997) detected four point-like sources, three in NGC 4490 and one in NGC 4485. The galaxy pair was subsequently observed three times with the *ROSAT* HRI in 1995 and 1996. Analyzing two of those observations, Roberts & Warwick (2000) only found one additional point source, an apparently transient source coincident with NGC 4490. Liu & Bregman (2005) analyzed all three *ROSAT* observations as part of their study of ULXs using the *ROSAT* HRI archive. They found the same sources as Roberts & Warwick (2000). Most recently, the system was observed three times with *Chandra* between 2000 and 2004 and once with *XMM-Newton* in 2002. Analyzing the first of the *Chandra* observations, Roberts et al. (2002) found 31 point sources, 29 of those being coincident with NGC 4490, one coincident with NGC 4485, and one source located in a bridge between the galaxies.

The *Chandra* observations of the NGC 4485/90 system are summarized in Table 4. These are all ACIS-S full-frame imaging observations taken in Timed Exposure mode. The frame time was in all cases set at the standard value of 3.2 s, and events were telemetered in either the Faint or Very Faint formats. The observations span a period of about 4 yr and have a cumulative good live exposure time of 97.5 ks. In all three observations all the sources coincident with NGC 4485/90 fall within the S3 chip.

The data were analyzed as described in § 2. Source detection was performed on a  $8.8' \times 8.7'$  rectangle encompassing the system. A total of 38 reliable source detections down to a luminosity of  $\sim 1 \times 10^{37} \text{ ergs s}^{-1}$  were found to be coincident with the two galaxies. Of these, 33 are coincident with NGC 4490, three coincident with NGC 4485, and two more are located in the bridge between the galaxies (see Fig. 1). The source catalog is presented in Table 10. An adaptively smoothed color-coded image based on the co-added *Chandra* exposure is shown in Figure 2.

Of the 38 sources, 27 had previously been detected by Roberts et al. (2002) and 11 had not been seen before. In addition, four of the sources reported in Roberts et al. (2002) fell below our threshold of detection significance and are therefore not included in our tables. Comparing our source locations to the USNO-A2.0 Catalogue (Monet et al. 1998), we find no close matches between the locations of foreground stars and our detected sources. There have been two historical supernovae in NGC 4490: SN 1982F, which is not detected, and recently SN 2008ax.

We estimate how many of our detections can be ex-

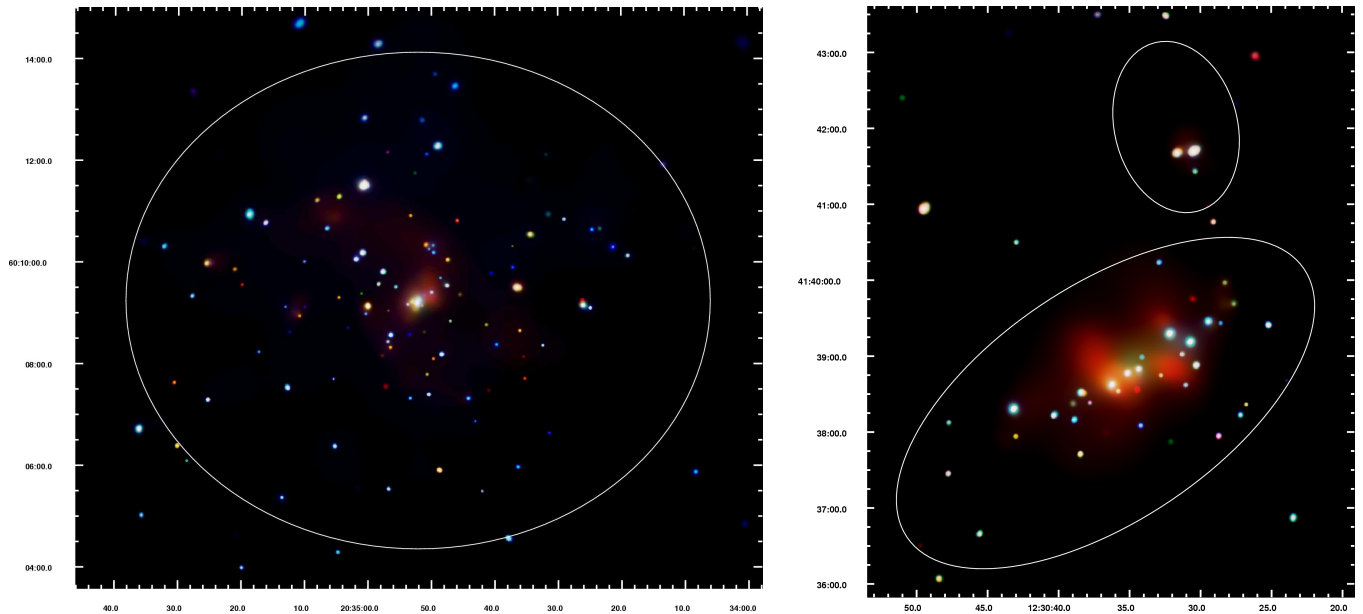


FIG. 2.— Adaptively smoothed color-coded images based on the co-added *Chandra* exposures of NGC 6946 (*left*) and NGC 4485/4490 (*right*). Red corresponds to X-rays with energies 0.3 – 1 keV, green to 1 – 2 keV, and blue to 2 – 7 keV.

pected to arise from CBSs using the same procedure as the one described for NGC 6946 in § 3.1. We use the results of Clemens et. al (1998) to estimate that a typical absorption column through the NGC 4485/90 system is  $\sim 3.5 \times 10^{21} \text{ cm}^{-2}$ , giving a total absorption column of  $\sim 3.7 \times 10^{21} \text{ cm}^{-2}$  for CBSs behind NGC 4485/90. Applying the formulae of Bauer et al. (2004) then yields an estimate of  $\sim 5$  for the expected number of CBSs among our 38 detected sources. For comparison, we note that Roberts et al. (2002), using the results of Giacconi et al. (2001), attribute  $< 4.5$  of their detections to CBSs.

The *ROSAT* HRI and *XMM-Newton* EPIC observations of NGC 4485/90 are summarized in Tables 5 and 6. The first of the *ROSAT* observations is too short to be of significant use to this study, and it is not included in Table 5.

#### 4. PROPERTIES OF THE SOURCE POPULATIONS

##### 4.1. Flux Variability

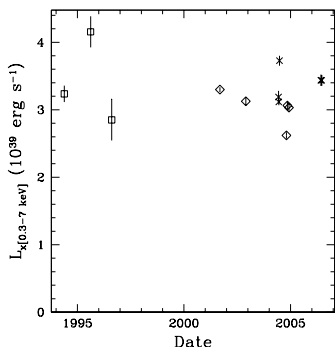


FIG. 3.— Long-term light curve of the ULX in NGC 6946 (CXOU J203500.7+601130). Diamonds represent *Chandra* ACIS observations, crosses represent *XMM-Newton* EPIC observations, and squares represent *ROSAT* HRI observations.

The variability properties of the sources in NGC 6946 are summarized in Table 11. Based on the source flux variability parameter  $S_{\text{flux}}$  defined in § 2.4 we classify 25 of the 85 nonforeground sources, or 29%, as variable on timescales of weeks, months, or years. Of these, 17 sources are seen to vary by more than a factor of 2, and we classify 11 sources (or 13% of the 85) as transient candidates (two of those are recent supernovae). Evidence for short-term (hours) variability, as defined in § 2.4, is seen in four, or 5%, of the 85 sources. Two of those also show long-term variability. Unsurprisingly, none of the sources associated with SNRs from the lists of Matonick & Fesen (1997) and Lacey & Duric (2001) shows variability of any kind above a level of  $2\sigma$ , with the exception of the ULX (see § 4.2.2).

The variability properties of the sources in NGC 4485/90 are summarized in Table 12. We classify 15 of the 38 sources, or 39%, as showing variability on timescales of months or years. Of these, 10 sources vary by more than a factor of 2, and four sources (or 11% of the 38) are transient candidates. Evidence for short-term variability is seen in four of the 38 sources. All of those also show long-term variability.

Due to the limited number of counts within each observation for most of the sources showing short-term variability, it is very difficult (with one marginal exception) to draw any concrete conclusions about the nature of the variability (e.g., to distinguish between burst-like behavior and more continuous decline or rise in count rate). The brightest of these sources, CXOU J203500.1+600908 in NGC 6946, seems in the first *Chandra* observation to show a burst-like increase in count rate on a timescale of  $\sim 5 - 10$  ks superposed on a steady decline in count rate throughout the whole observation.

Where possible, the baseline of the long-term light curves of the ULXs was extended by adding data points from *ROSAT* HRI and *XMM-Newton* observations as described in § 2.5. Long-term light curves of the 10 brightest sources in NGC 6946 are shown in Figures 3 and 4,



TABLE 6  
*XMM-Newton* EPIC OBSERVATION OF NGC 4485/4490

Start Date	Obs. ID	MOS-1		MOS-2		PN	
		Exp. <sup>a</sup> (ks)	Mode <sup>b</sup> / Filter <sup>c</sup>	Exp. (ks)	Mode/ Filter	Exp. (ks)	Mode/ Filter
2002 May 27	0112280201	16.34	FF-ME	16.37	FF-ME	11.17	EFF-ME

<sup>a</sup> Good live exposure time.

<sup>b</sup> Instrument modes: FF = full frame, EFF = extended full frame.

<sup>c</sup> Filters: ME = medium filter.

and of the 10 brightest sources in NGC 4485/90 in Figures 5 and 6. We emphasize that the error bars in the light curves contain only the  $1\sigma$  Poisson errors in the counts. The *ROSAT* and *XMM-Newton* data are generally of much lower quality than the *Chandra* data, and comparisons of luminosities between different instruments should be regarded with some caution. Various factors (e.g., cross-calibration issues and uncertainties in instrument responses and in assumed spectral shapes for energy conversions) are likely to add to the errors. To give some idea of the magnitude of additional errors we note that the *Chandra* team estimates<sup>10</sup> that present  $1\sigma$  calibration uncertainties for ACIS are 0.3% in the absolute energy scale, 5% in the absolute effective area, and a few percent for the relative efficiency (i.e., for variations in quantum efficiency over the area of the detector). When choosing a spectral model to use for calculating ULX fluxes (as described in § 2.2) the scatter in flux values between several well-fitting models was typically of the order of a few percent. However, sometimes none of the eight simple spectral models considered provided a particularly good fit, in which case the errors added are likely greater. As for cross-calibration uncertainties between *Chandra* and *XMM-Newton*, we expect that the relative cross-calibration error between our *Chandra* and *XMM-Newton* fluxes should likely be  $\lesssim 10\%$  (H. Marshall, private communication, 2008).

The observed fractions here of  $\sim 30\% - 40\%$  of sources showing flux variability is similar to what has been found in previous studies of late-type galaxies. Kilgard et al. (2005) survey 11 nearby face-on spiral galaxies with two *Chandra* observations each and find that at least 27% of the total number of sources exhibit variability on either long or short timescales. Grimm et al. (2007) analyze three observations of M33 and find that 25% of the detected sources exhibit long-term variability. They also classify 17% of their sources as candidate transients, similar to what is seen in our galaxies. Overall, the abundant variability observed among the sources in NGC 6946 and NGC 4485/90 clearly points to source populations dominated by accreting XRBs.

It is interesting to compare the number of transient candidates seen in NGC 6946 and NGC 4485/90 to the number in our own Galaxy. Inspection of the data archives of the *Rossi X-Ray Timing Explorer's All-Sky Monitor* (RXTE ASM) reveals that on average  $\sim 4$  transients (including recurrent ones) with luminosities above  $\sim 10^{37}$  ergs  $s^{-1}$  go off every year in the Galaxy (R. Remillard, private communication, 2008). We see 11 transient candidates in NGC 6946 and four

in NGC 4485/90 (all with maximum luminosities above  $10^{37}$  ergs  $s^{-1}$ ). Due to the close monitoring of our Galaxy by the ASM, we would expect it to reveal a larger fraction of the actual number of transients among the X-ray sources than a handful of *Chandra* observations do in NGC 6946 and NGC 4485/90. However, a large fraction of the transient population of the Milky Way is presumably obscured by gas and dust. To put these numbers in context, we compare the estimated masses and star formation rates of these systems. A typical quoted value for the dynamical mass of the Milky Way within  $\sim 20$  kpc is a few times  $10^{11} M_{\odot}$  (see, e.g., Nikiforov et al. 2000), and a recent estimate of its star formation rate is  $\sim 4 M_{\odot} \text{ yr}^{-1}$  (Diehl et al. 2006). Corresponding numbers for NGC 6946 and NGC 4485/90 are given in §§ 3.1 and 3.2. In short, the three systems are estimated to have similar star formation rates, and the Milky Way and NGC 6946 have comparable estimates for their mass, whereas NGC 4485/90 seems to be about an order of magnitude less massive.

## 4.2. Individual Sources

### 4.2.1. Historical Supernovae in NGC 6946

As mentioned in § 3.1, NGC 6946 has been host to nine historical supernovae, the most recent one being SN 2008S. The last three of the five *Chandra* observations were aimed at Type IIP SN 2004et and observed it 30, 45, and 72 days after the explosion (see light curve in Fig. 4). A multiwavelength study of this object in X-ray, optical, and radio is presented in Misra et al. (2007). Another *Chandra* study of SN 2004et is presented in Rho et al. (2007).

The second *Chandra* observation of NGC 6946, on 2002 November 25, was aimed at Type IIP SN 2002hh and observed it  $\sim 28$  days after the explosion, whose time is constrained to have been between 2002 October 26.1 and 31.1 UT (Li 2002). The measured luminosity at our adopted distance was  $\sim 3 \times 10^{38}$  ergs  $s^{-1}$ , with hardness ratios of  $HR1 = 0.09 \pm 0.03$  and  $HR2 = 0.78 \pm 0.12$ . No source was detected at the position of the supernova in the first *Chandra* observation in 2001 September. In the last three *Chandra* observations, made around two years after the explosion, the source is seen to be emitting at a luminosity of  $\sim 3 \times 10^{37}$  ergs  $s^{-1}$  (see light curve in Fig. 4). There is not a measurable difference in the soft color compared to the 2002 observation. However, the hard color exhibits significant softening between the 2002 and 2004 observations, being measured at  $HR2 = 0.39 \pm 0.23$ ,  $0.13 \pm 0.22$ , and  $-0.11 \pm 0.22$  in 2004. We note that SN 2004et exhibits similar spectral behavior, the soft color remaining constant but the hard color

<sup>10</sup> See <http://cxc.harvard.edu/cal/>.

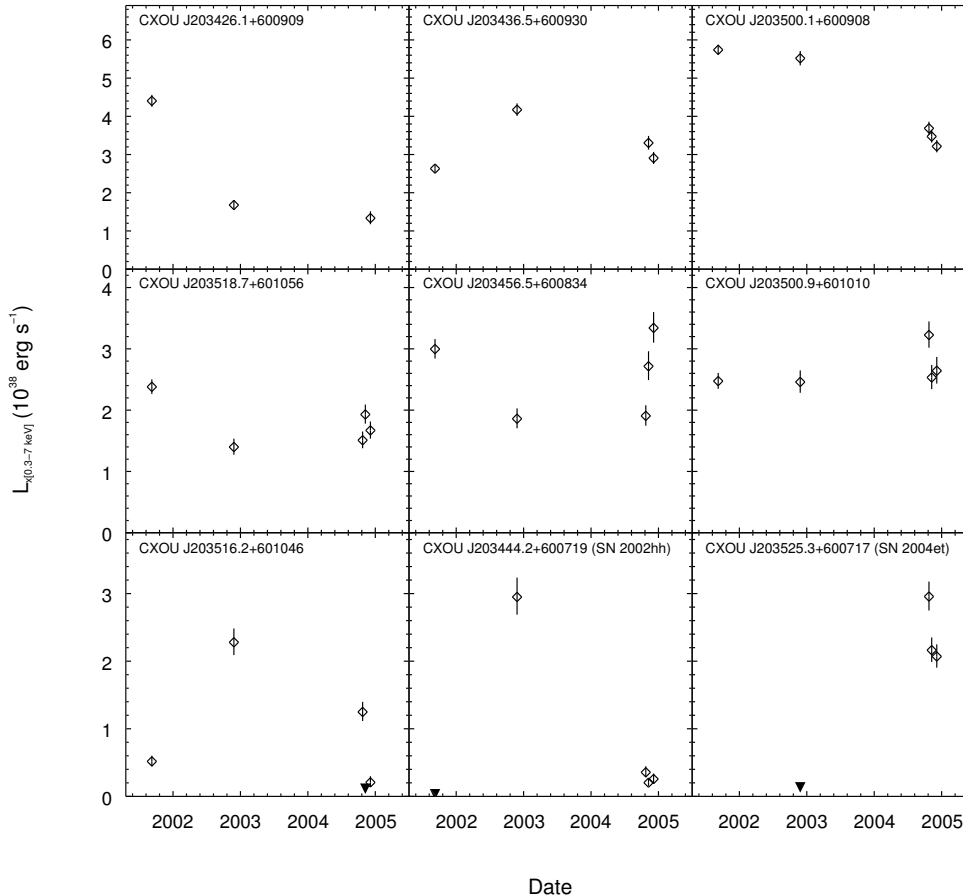


FIG. 4.— Long-term *Chandra* light curves of nine of the most luminous sources in NGC 6946. Filled downward triangles represent upper limits with  $3\sigma$  Gaussian confidence.

decreasing (see entries in Tables 13 and 14), although the hard color is never seen to be as high as in the first observation of SN 2002hh. This is in agreement with the finding of Misra et al. (2007) for SN 2004et that, while the 2 – 8 keV flux decays, the 0.5 – 2 keV flux remains roughly constant.

Type III SN 1980K fell outside the detector in the first *Chandra* observation but is seen to be emitting steadily at  $\sim 3 \times 10^{37}$  ergs  $s^{-1}$  in the other four observations. We note that it was observed by the *Einstein* IPC 35 and 82 days after maximum light (which was  $\sim 15$  days after the explosion). From those observations Canizares et al. (1982) report absorption corrected luminosities of  $\sim 7 \times 10^{38}$  ergs  $s^{-1}$  and  $\sim 4 \times 10^{38}$  ergs  $s^{-1}$  in the 0.2 – 4 keV band (after scaling their values to our adopted distance). SN 1980K was also observed by the *ROSAT* PSPC in 1992 June. Schlegel (1994c) gives a luminosity estimate of  $\sim 2 \times 10^{37}$  ergs  $s^{-1}$  in the 0.5 – 2 keV range (scaled to our adopted distance). Type II SN 1968D is seen in all five *Chandra* observations and has a luminosity of  $\sim 2 \times 10^{37}$  ergs  $s^{-1}$ . The other four historical supernovae (SN 1917A, SN 1939C, SN 1948B, and SN 1969P) are not detected.

#### 4.2.2. U LX in NGC 6946

The only ultraluminous X-ray source in NGC 6946, often called MF16 (Matonick & Fesen 1997), has been ex-

tensively studied. It was first detected with the *Einstein* IPC in 1979–1981 (Fabbiano & Trinchieri 1987) and was later observed with the *ROSAT* PSPC in 1992. Analyzing the *ROSAT* observation, Schlegel (1994a) derived an X-ray luminosity of  $3.7 \times 10^{39}$  ergs  $s^{-1}$  in the 0.5 – 2 keV band (scaled to our adopted distance), and identified the source as a supernova remnant based on an optical counterpart discovered by Blair & Fesen (1994). The remnant appears to be quite evolved, perhaps  $\sim 10^3 - 10^4$  yr old (Blair & Fesen 1994; Dunne et. al 2000; Blair et al. 2001). *Hubble Space Telescope* images presented by Blair et al. (2001) reveal a three loop structure with an extent of  $1.4'' \times 0.8''$  (corresponding to  $39 \times 23$  pc at our adopted distance). Various models have been put forward to try to explain this unusually high luminosity from such an evolved SNR. Blair et al. (2001) propose that ejecta from a young supernova might be interacting with the dense shell of an older SNR; Dunne et. al (2000) suggest instead that a single supernova blast wave is interacting with a dense circumstellar nebula from a high-mass progenitor and that a hard spectral component in the *ROSAT* PSPC data comes from a pulsar wind nebula. Schlegel et al. (2003), analyzing the first *Chandra* observation, argue from spectral considerations that neither of these scenarios can explain the data. Roberts & Colbert (2003) analyze the first two *Chandra* observations of the object and speculate that the luminosity of MF16 arises

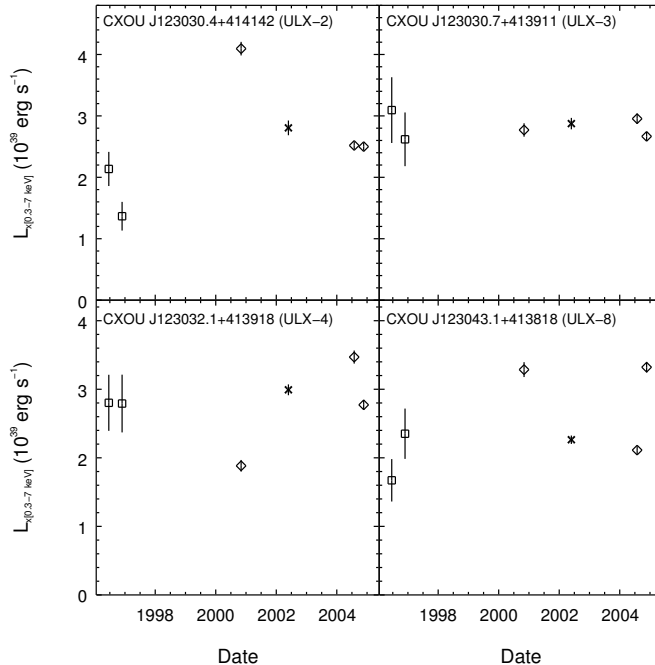


FIG. 5.— Long-term light curves of the four most luminous sources in NGC 4485/90. Diamonds represent *Chandra* ACIS observations, crosses represent *XMM-Newton* EPIC observations, and squares represent *ROSAT* HRI observations.

from a black hole X-ray binary (BHXR) within the SNR. They argue this based on (1) the point-like nature of the X-ray source, (2) the close resemblance of the source spectrum to spectra from other ULXs thought to be BHXR, (3) the short-timescale (minutes) variability of the hard component (1.1 – 10 keV) of the flux, and (4) the long-timescale drop of  $\sim 13\%$  in count rate between the first and second *Chandra* observations ( $\sim 3\%$  thereof stemming from a degradation in effective area). Our K-S test does not detect short-timescale variations in the full 0.3 – 7 keV band for any of the *Chandra* observations. We do, however, see definite long-term variability in the *Chandra* data (see light curve in Fig. 3). There is a drop in luminosity of  $\sim 5\%$  between the first and second observations, and then a much larger drop between the second and third observations; the luminosity in the third observation is  $\sim 79\%$  of the original first observation value. Two weeks later, in the fourth *Chandra* observation, the luminosity has again increased to  $\sim 93\%$  of its original value. We also see clear evidence of variability in the *XMM-Newton* data, most notably a  $\sim 20\%$  jump in luminosity in the 12 days between two observations in 2004 June. Finally, we see variations in the soft color with a significance of  $2.9\sigma$  (see Fig. 7). These spectral variations do not seem to have a clear correlation with flux. There is spectral softening associated with the drop in flux between the second and third *Chandra* observations, but there is no detectable hardening when the flux subsequently increases again. Overall, this observed variability considerably strengthens the case for an accreting object as the source of at least part of the X-ray emission from MF16.

#### 4.2.3. ULXs in NGC 4485/4490

The NGC 4485/90 system contains a high number of ULXs, a total of eight. In a comprehensive survey of nearby galaxies observed with the *ROSAT* HRI, Liu et al. (2006, see also Liu & Bregman 2005) find an average rate of  $\sim 0.5$  ULXs per galaxy. The rate is higher when only considering late-type galaxies and still higher for starburst galaxies ( $\sim 1.0$ ). Considerably higher numbers, however, are not unusual for interacting galaxies (see, e.g., Brassington et al. 2007), an extreme case being the Antennae, with 14 known ULXs (Zezas et al. 2006).

Seven of the ULXs in the NGC 4485/90 system are in NGC 4490 and one is in NGC 4485. We numerate them here in order of right ascension (see Table 10). Two of them, ULX-5 and ULX-7, have not been identified as being ultraluminous before, their luminosities having entered the ULX range only in the most recent *Chandra* observation.

The maximum luminosities of the ULXs range from  $1.0 \times 10^{39}$  ergs  $s^{-1}$  to  $4.1 \times 10^{39}$  ergs  $s^{-1}$ . These sources show a lot of variability. Long-term flux variability above the  $3\sigma$  level is exhibited by all but one of them (see light curves in Figs. 5 and 6). ULX-7 is a transient, ULX-5 varies by a factor of  $\sim 11$  and ULX-6 by a factor of  $\sim 5$ . The others vary by less than a factor of 2. ULX-5 shows short-term flux variability. Two sources, ULX-6 and ULX-8, have significant variations in their hard color. In both cases, there is a clear transition from a harder higher luminosity state to a softer lower luminosity one and back (see Fig. 7).

Vazquez et al. (2007) use the Infrared Spectrograph on the *Spitzer Space Telescope* to do mid-infrared spectral diagnostics on six of the ULXs (all except ULX-5 and ULX-7). They find that five of those show ionization features that they claim indicate accretion, whereas the sixth source, ULX-1, seems to be more con-

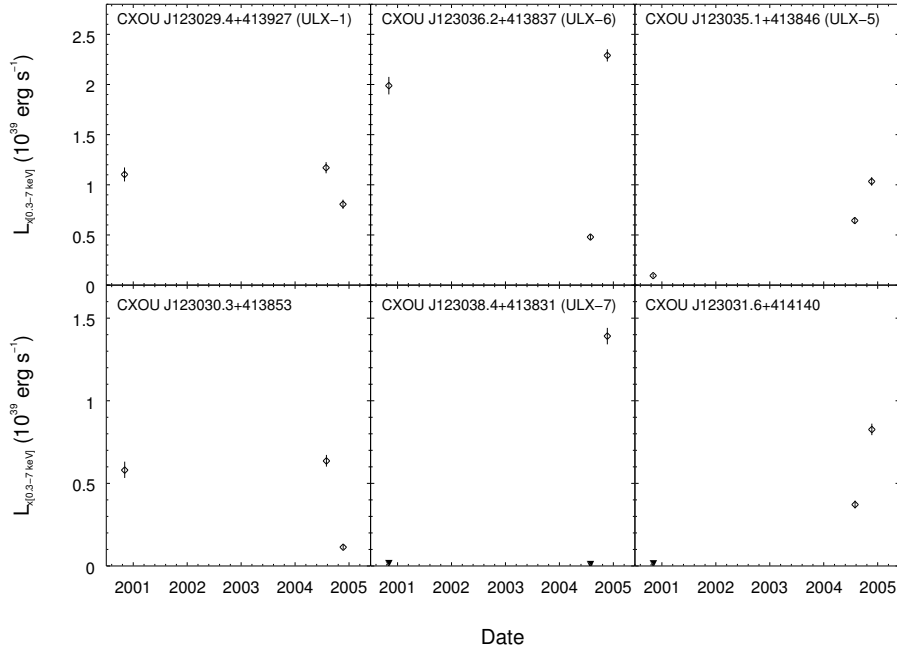


FIG. 6.— Long-term *Chandra* light curves of six of the most luminous sources in NGC 4485/90. Filled downward triangles represent upper limits with  $3\sigma$  Gaussian confidence.

sistent with a SNR. As pointed out by Roberts et al. (2002), ULX-1 is coincident with a radio source, FIRST J123029.4+413927, which also points towards a SNR origin for ULX-1. However, we see a  $\sim 30\%$  drop in luminosity in the four months between the second and third *Chandra* observations—behavior that is more typical of an accreting XRB than a SNR. This is reminiscent of the ULX in NGC 6946, which has also been associated with a SNR but whose X-ray variability indicates an accreting XRB.

The abundance of variability among the ULXs in NGC 4485/90 is similar to what is seen in the Antennae. Zezas et al. (2006) find that two of the ULXs in the Antennae show variability on a timescale of a few days. Twelve out of 14 ULXs show long-term variability, one being a transient, and four of the ULXs occasionally have luminosities below the ULX limit. In NGC 4485/90 we find that four of the eight ULXs have a luminosity below  $10^{39}$  ergs  $s^{-1}$  in at least one of the three *Chandra* observations. It is therefore clear that a single observation of a galaxy is by no means guaranteed to discover the galaxy’s full ULX population. Surveys such as that of Liu et al. (2006), where many of the galaxies are only observed once or twice, can only give a lower limit to the average number of sources in a galaxy with the potential of being ultraluminous at one time or other.

### 4.3. Hardness Ratios

#### 4.3.1. Variability

The hardness ratios of the sources in NGC 6946, both for each observation and for the co-added exposure, are given in Tables 13 and 14. The hardness ratios for the NGC 4485/90 sources are similarly given in Table 15. Significance parameters for variability in the hardness ratios between observations are given in Tables 11 (NGC 6946) and 12 (NGC 4485/90). Variability above  $3\sigma$  in ei-

ther of the ratios is only detected in two of the sources in NGC 6946 and three of the sources in NGC 4485/90. In addition, the ULX in NGC 6946 shows a  $2.9\sigma$  variation in its hard color. We note that a much larger fraction of the sources probably undergoes some spectral variation, but most of the sources have too few counts for the hardness ratios to be very sensitive to spectral changes. Color-luminosity plots for the sources exhibiting significant hardness ratio variability are shown in Figure 7. Four of these sources (one of those being SN 2002hh) seem to show a clear correlation between higher luminosity and increased hardness, whereas the other two show more complicated behavior. Previous studies of external galaxies have routinely found sources with spectral variability, in some cases with spectral behavior reminiscent of Galactic XRBs; flux-color transitions have also been observed in ULXs (Fabbiano 2006 and references therein). Zezas et al. (2006) find signs of variability in hardness ratios of 21 of their  $\sim 70$  detected sources in the Antennae; some of these are ULXs. As in our case, they find that the variability does not follow the same pattern for all sources. They see sources that become harder with higher luminosity, as we do, but also sources that soften with increased luminosity. In addition, some of the sources show no regular pattern, or no significant variation in luminosity.

#### 4.3.2. Supersoft Sources

Two sources have especially soft spectra and are strong candidates for supersoft sources (SSSs; see, e.g., Di Stefano & Kong 2003). CXOU J203426.2+600914 in NGC 6946 has all of its 68 source counts below 1 keV, and CXOU J123034.5+413834 in NGC 4490 has 32 of its total 35 source counts below 1 keV, 25 counts being below 0.65 keV. Both sources have a luminosity of  $\sim 9 \times 10^{36}$  ergs  $s^{-1}$ , and neither one shows evidence for

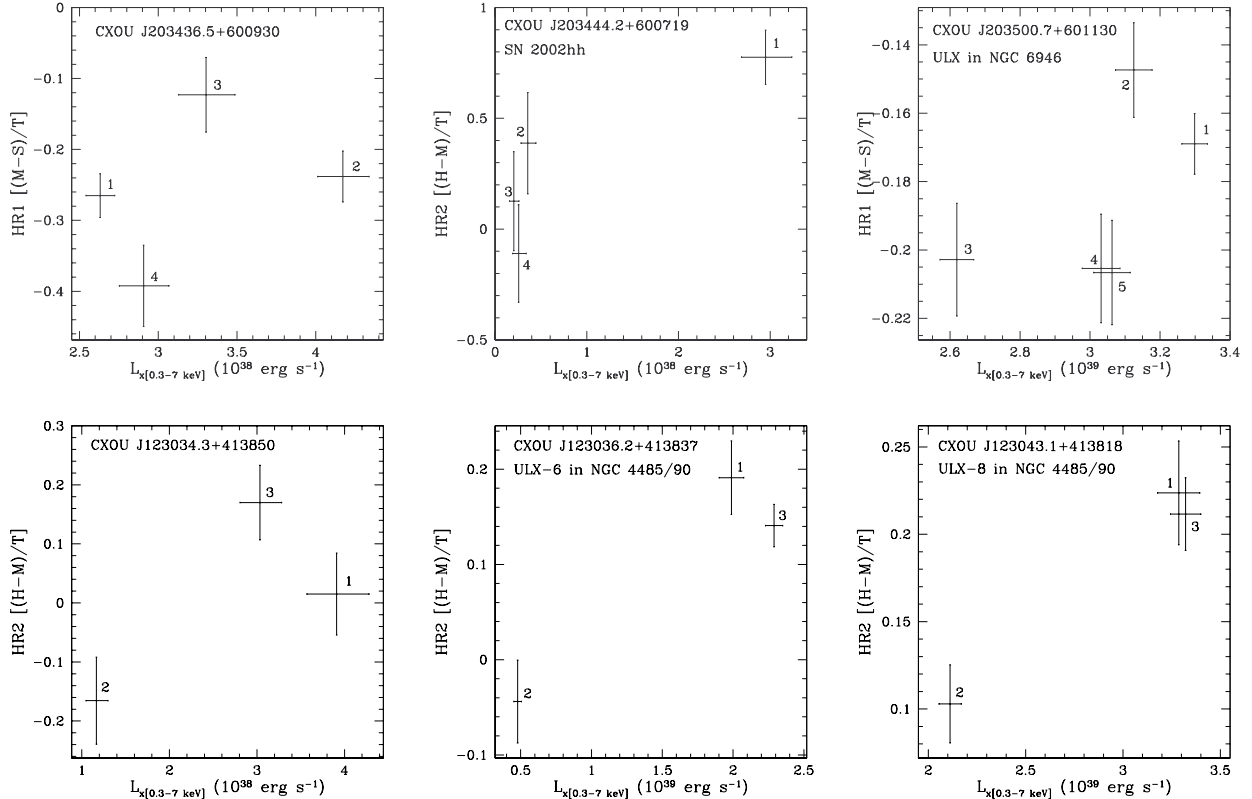


FIG. 7.— Soft or hard color as a function of luminosity for sources that show significant variation in their hardness ratios. Numbers next to data points indicate their order in time.

variability.

#### 4.3.3. Spectral Classification

Color-color diagrams for the sources in NGC 6946 and NGC 4485/90, based on the co-added exposures, are shown in Figure 8. The fact that most of the sources do not show significant variation in their hardness ratios between observations provides justification for using hardness ratios calculated from the co-added exposure to describe the source populations’ spectral properties. The classification scheme of Prestwich et al. (2003) discussed in § 2.3, is overlaid. As mentioned before, although a source’s position in a color-color diagram does not give conclusive information about the nature of the source, the overall distribution of sources should give us some information about the population as a whole. Also indicated in the color-color diagrams is the physically allowed region, covering all combinations of HR1 and HR2 possible if the net counts in all the energy bands (S, M, H, T; see § 2.3) are non-negative. Due to background subtraction in cases of very few source counts, some of the hardness ratios fall outside this region. They are, however, all consistent with the physically allowed region within their  $1\sigma$  errors.

Prestwich et al. (2003) note that, while thermal SNRs are in general expected to have  $-0.9 < \text{HR1} < -0.4$ , as indicated in the classification scheme, SNRs whose spectra are dominated by nonthermal components will have somewhat harder spectra and are likely to be located in the LMXB or even absorbed sources part of the color-color diagram. We see in Figure 8 that the locations of

the sources associated with SNRs in NGC 6946 are in good agreement with this.

For NGC 4485/90, all but two of the 38 sources fall in the XRB regions of the color-color diagram, with roughly equal portions falling in the LMXB and HMXB regions. In NGC 6946 there seems to be a much larger SNR component to the population. In addition to the four detected historical supernovae and the six sources associated with optically or radio identified SNRs,  $\sim 5$  sources have colors consistent with thermal SNRs. The rest of the sources in NGC 6946 (apart from the SSS candidate) have colors consistent with XRBs, again with roughly equal portions in the LMXB and HMXB regions. We note that a large portion of the sources has colors consistent with both regions. The large presence of HMXBs in these systems, indicated by the color-color diagrams, is not surprising given the high level of star formation observed.

All the ULXs have colors consistent with XRBs. The ULX in NGC 6946 falls firmly in the LMXB region, whereas six of the ULXs in NGC 4485/90 have colors more consistent with HMXBs. Variable and transient sources are equally divided between the LMXB and HMXB regions in NGC 4485/90. For NGC 6946, these sources seem to slightly favor the LMXB region, but this is hardly a significant difference. The most variable sources (those that vary by a factor of 10 or more) are also seen to be roughly equally divided between the LMXB and HMXB regions in both galaxies.

#### 4.4. Luminosity Functions

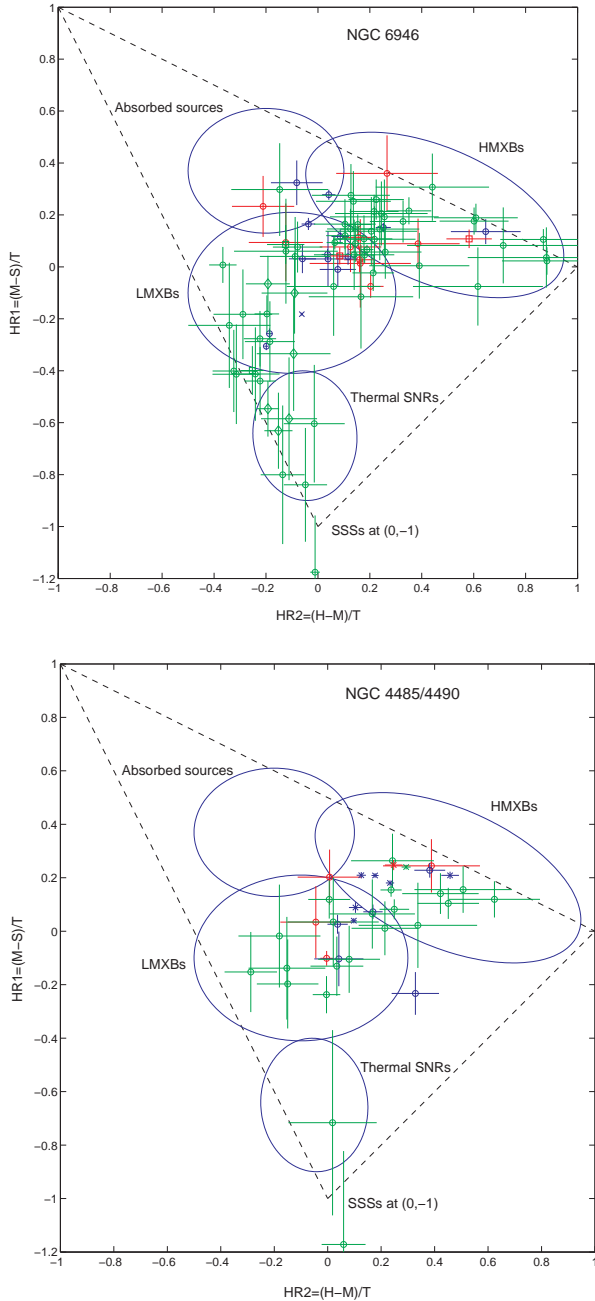


FIG. 8.— Color-color diagrams for the sources in NGC 6946 and NGC 4485/4490 based on the co-added *Chandra* exposures. The classification scheme of Prestwich et al. (2003) is overlaid. Historical supernovae are represented with boxes, SNRs with diamonds, ULXs with crosses, and other sources with circles. Blue indicates that long-term variability is detected, green that it is not, and red denotes transient candidates. The triangle enclosed by the dashed lines represents the physically allowed region where net counts in all energy bands are non-negative. Due to background subtraction, faint sources can fall outside this region.

We construct X-ray luminosity functions (XLFs) for each observation, as well as the co-added exposure, of both NGC 6946 and NGC 4485/90. We use luminosities from the full 0.3–7 keV band. In the case of NGC 6946, where parts of the galaxy fell outside the *Chandra* detectors in each observation, only sources that fell within the

TABLE 7  
POWER-LAW INDICES OF  
THE XLFs OF NGC  
6946

Obs.	$\alpha^a$
1043	$0.61 \pm 0.13$
4404	$0.63 \pm 0.10$
4631	$0.67 \pm 0.11$
4632	$0.72 \pm 0.13$
4633	$0.67 \pm 0.12$
Co-added	$0.73 \pm 0.14$

<sup>a</sup> Best-fit cumulative slope. Uncertainties given are estimated 90% confidence intervals.

detectors in all five observations were considered. Hence, 24 of the 85 nonforeground sources were discarded. This was done to make sure that when comparing the XLFs from different observations we are comparing the same source population.

To avoid any effects of incompleteness at the low-luminosity end of the XLF, we set a conservative completeness limit for both galaxies and consider only the portion of the XLF above that limit. To facilitate comparisons between different observations we use the same completeness limit for all observations of each galaxy. We fit a simple power law to the unbinned distribution for each observation using the Cash statistic (Cash 1979). In order to test the null hypothesis that the XLFs of different observations of the same galaxy are derived from the same parent distribution, we compare the XLFs in pairs using a two-sided Kolmogorov-Smirnov test.

The XLFs for NGC 6946 are shown in Figure 9. We adopt a completeness limit of  $2 \times 10^{37}$  ergs s<sup>-1</sup>. Judging from the figure, the XLF of the galaxy does not seem to vary much between observations. This is borne out by the results of the pairwise K-S tests between the five individual observations, which yield significance levels ranging from 0.52 to 0.99 and thus do not warrant rejection of the null hypothesis of a common parent distribution. Interestingly, performing the K-S test between the co-added exposure and each of the observations, we get lower significance levels, ranging from 0.13 to 0.77. The best-fit cumulative slopes of the XLFs are shown in Table 7. They are in all cases  $\sim 0.6-0.7$  and are in good agreement with each other. We note that Holt et al. (2003) derive a slope of  $0.68 \pm 0.03$  for the first *Chandra* observation, in agreement with our value of  $0.61 \pm 0.13$ .

The XLFs for NGC 4485/90 are shown in Figure 9. Here we adopt a completeness limit of  $4 \times 10^{37}$  ergs s<sup>-1</sup>. Again, there does not seem to be significant variation between individual observations. This is supported by pairwise K-S tests between the three observations, which yield significance levels from 0.58 to 0.97. Performing the K-S test between the co-added exposure and individual observations yields higher significance levels here (between 0.93 and 0.98), in contrast to NGC 6946. The best-fit cumulative slopes of the XLFs shown in Table 8 agree well with each other and are all  $\sim 0.4-0.5$ . We note that Roberts et al. (2002) derive a slope of  $0.57 \pm 0.10$  for the first *Chandra* observation, in agreement with our value of  $0.45 \pm 0.10$ . There is an indication in Figure 9

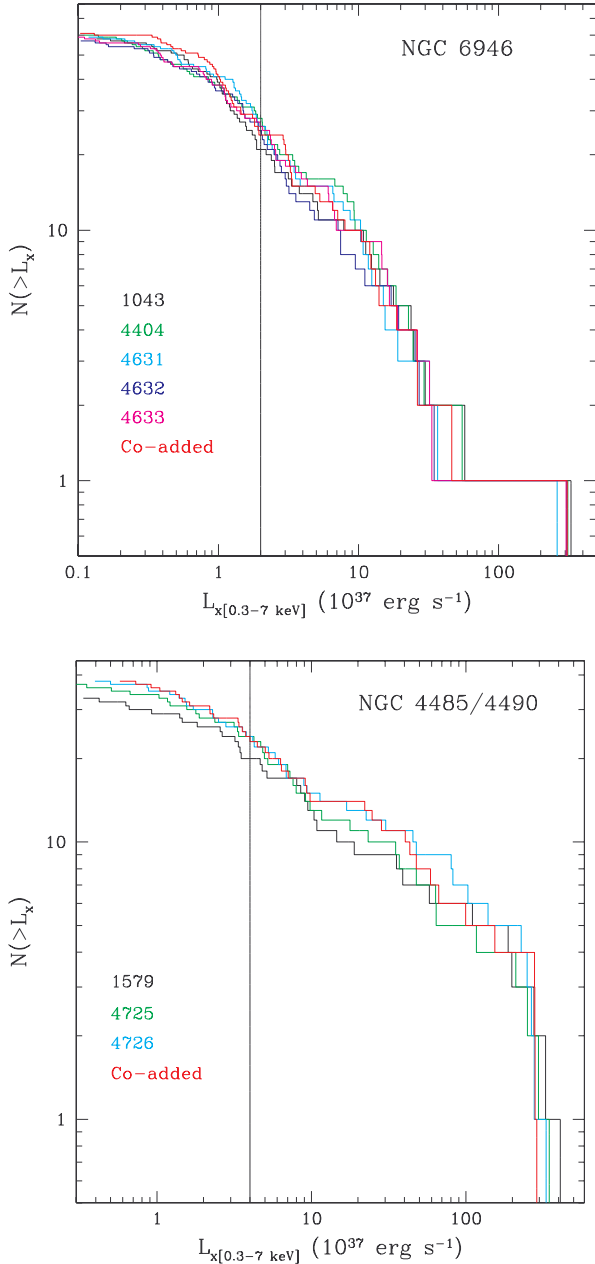


FIG. 9.— Cumulative X-ray luminosity functions for all the *Chandra* observations and the co-added exposures of NGC 6946 and NGC 4485/4490. The vertical lines show the adopted completeness limits.

of a high-luminosity break or cutoff in the XLFs, which steepen considerably for the  $\sim 3$  most luminous sources. We therefore also tried fitting a broken power law to the XLFs. This typically led to a best-fit break luminosity of  $\sim (2 - 3) \times 10^{39}$  ergs  $s^{-1}$  and a slope for the low-luminosity portion that is  $\sim 0.05$  lower than for the simple unbroken power law (i.e.,  $\sim 0.4$ ). The slope of the high-luminosity portion was, however, in all cases very poorly constrained.

We use the results of Bauer et al. (2004) to assess whether CBSs are likely to have a significant effect on the XLFs. In NGC 6946 we expect  $\sim 8$  CBSs among the  $\sim 25$  sources typically above the completeness limit

TABLE 8  
POWER-LAW INDICES OF  
THE XLFs OF NGC  
4485/90

Obs.	$\alpha^a$
1579	$0.45 \pm 0.10$
4725	$0.49 \pm 0.09$
4726	$0.42 \pm 0.08$
Co-added	$0.45 \pm 0.08$

<sup>a</sup> Best-fit cumulative slope. Uncertainties given are estimated 90% confidence intervals.

and within the region covered by all five *Chandra* observations. In NGC 4485/90 we estimate that  $\sim 3$  of the  $\sim 23$  sources typically above the completeness limit can be expected to be CBSs. Based on these numbers alone, one might expect that CBSs could have a significant effect in the case of NGC 6946 but probably only a small effect for NGC 4485/90. As it turns out, the cumulative number-flux slopes for CBSs derived in Bauer et al. (2004) are quite similar to the ones for the XLFs: 0.55 for the 0.5 – 2 keV band and 0.56 for the 2 – 8 keV band. Contamination of our sample by CBSs is therefore likely to have only a small effect in both cases. The true slopes for NGC 4485/90 are probably slightly flatter than those derived above and slightly steeper for NGC 6946. However, the change in XLF slopes due to CBSs is almost certainly well within the uncertainties quoted in Tables 7 and 8.

Our results agree well with previous results for other galaxies. As mentioned in § 1, XLFs have been seen to be remarkably stable in spite of variability among individual sources, and NGC 6946 and NGC 4485/90 do not seem to be an exception. Single-observation snapshots of their XLFs therefore seem to represent rather well their shape averaged over longer times. Their cumulative XLF slopes fall firmly in the regime of starburst galaxies, whose slopes are typically between 0.4 and 0.8 (Fabbiano 2006)—another clear indication of the young stellar populations in these two systems.

## 5. SUMMARY AND CONCLUSIONS

We have presented a study of the X-ray source populations in the spiral galaxy NGC 6946 and the irregular/spiral interacting galaxy pair NGC 4485/4490. We analyzed data from five *Chandra* observations of NGC 6946 and from three *Chandra* observations of NGC 4485/90. We detect 90 point sources coincident with NGC 6946 (excluding a small circumnuclear region) down to luminosities of a few times  $10^{36}$  ergs  $s^{-1}$ . We associate five of these with foreground stars. Seven sources are coincident with optically or radio identified SNRs, and four are supernovae from the past 40 years. We detect 38 sources coincident with NGC 4485/90 down to a luminosity of  $\sim 1 \times 10^{37}$  ergs  $s^{-1}$ .

In NGC 6946, 25 of the 85 sources exhibit long-term (weeks to years) variability in luminosity; 11 are transient candidates. We detect short-term (hours) variability in four sources. Three sources show significant variability in their hardness ratios. We find that the single ULX

in NGC 6946, the SNR known as MF16, exhibits long-term variability in flux and color that strongly supports speculations of its high luminosity arising from an XRB within the remnant.

In NGC 4485/90, 15 of the 38 sources show flux variability on timescales of months to years; four are transient candidates. Short-term variability is seen for four sources, and three show variability in their hardness ratios. NGC 4485/90 contains eight ULXs. Two of these have not been identified as ULXs before; this shows the value of long-term monitoring in identifying ultraluminous sources. All but one of the ULXs exhibit long-term variability, and one of them is a transient. One of the ULXs, which has been associated with a SNR based on spectral characteristics and its spatial coincidence with a radio source, shows clear long-term variability pointing to an accreting XRB. We detect short-term variability for one ULX, and two have significant variations in color. This abundant variability among the ULXs clearly points to accretion as the source of luminosity.

Consistent with the widespread variability seen within the source populations, the X-ray colors of the sources indicate that the populations are dominated by XRBs. The source population of NGC 6946 also seems to contain a sizable SNR component, perhaps  $\sim 15\% - 20\%$  of the

detected sources. The distribution of colors among the sources in both NGC 6946 and NGC 4485/90 indicates roughly equal fractions of LMXBs and HMXBs. Such a significant presence of HMXBs is consistent with the fact that both systems show high star formation activity.

The shape of the XLFs of NGC 6946 and NGC 4485/90 does not change significantly between observations, and seems to be well represented by single-observation snapshots. The XLF of NGC 6946 (above  $2 \times 10^{37}$  ergs  $s^{-1}$ ) can be described by a power law with cumulative slope  $\sim 0.6 - 0.7$ . The XLF of NGC 4485/90 can be described by a power law with cumulative slope  $\sim 0.4$  between  $4 \times 10^{37}$  and  $2 \times 10^{39}$  ergs  $s^{-1}$ . Above  $\sim 2 \times 10^{39}$  ergs  $s^{-1}$ , the luminosity function drops off rather sharply. The flatness of the slopes (especially for NGC 4485/90) is another testament to the systems' high star formation rate and young stellar population.

This work was supported by *Chandra* Award AR6-7009X. Use was made of data obtained from the High Energy Astrophysics Science Archive Research Center (HEASARC), provided by NASA's Goddard Space Flight Center. We thank the referee for thorough reading of the paper and constructive comments.

#### REFERENCES

- Bauer, F. E., Alexander, D. M., Brandt, W. N., Schneider, D. P., Treister, E., Hornschemeier, A. E., & Garmire, G. P. 2004, *AJ*, 128, 2048
- Blair, W., & Fesen, R. 1994, *ApJ*, 424, L103
- Blair, W. P., Fesen, R. A., & Schlegel, E. M. 2001, *AJ*, 121, 1497
- Brassington, N. J., Ponman, T. J., & Read, A. M. 2007, *MNRAS*, 377, 1439
- Broos, P. S., Townsley, L. K., Getman, K., & Bauer, F. E. 2002, ACIS Extract, An ACIS Point Source Extraction Package (University Park: Pennsylvania State Univ.), [http://www.astro.psu.edu/xray/docs/TARA/ae\\_users\\_guide.html](http://www.astro.psu.edu/xray/docs/TARA/ae_users_guide.html)
- Canizares, C. R., Kriss, G. A., & Feigelson, E. D. 1982, *ApJ*, 253, L17
- Cash, W. 1979, *ApJ*, 228, 939
- Clemens, M. S., Alexander, P., & Green, D. A. 1998, *MNRAS*, 297, 1015
- . 1999, *MNRAS*, 307, 481
- . 2000, *MNRAS*, 312, 236
- Clemens, M. S., & Alexander, P. 2002, *MNRAS*, 333, 39
- Crosthwaite, L. P., & Turner, J. L. 2007, *ApJ*, 134, 1827
- David, L. P., et al. 1999, The *ROSAT* High Resolution Imager (HRI) Calibration Report (Cambridge: SAO)
- Davis, S. D., & Mushotzky, R. F. 2004, *ApJ*, 604, 653
- de Vaucouleurs, G. 1979, *ApJ*, 227, 729
- de Vaucouleurs, G., de Vaucouleurs, A., & Corwin, H. G., Jr. 1976, Second Reference Catalogue of Bright Galaxies (Austin: Univ. Texas Press)
- de Vaucouleurs, G., de Vaucouleurs, A., Corwin, H. G., Jr., Buta, R. J., Paturel, G., & Fouque, P. 1991, Third Reference Catalogue of Bright Galaxies (New York: Springer)
- Dickey, J. M., & Lockman, F. J. 1990, *ARA&A*, 28, 215
- Diehl, R., et al. 2006, *Nature*, 439, 45
- Di Stefano, R., & Kong, A. K. H. 2003, *ApJ*, 592, 884
- Dunne, B. C., Gruendl, R. A., & Chu, Y.-H. 2000, *AJ*, 119, 1172
- Eastman, R. G., Schmidt, B. P., & Kirshner, R. 1996, *ApJ*, 466, 911
- Elmegreen, D. E., Chromey, F. R., Knowles, B. D., & Wittenmyer, R. A. 1998a, *AJ*, 115, 1433
- Elmegreen, D. E., Chromey, F. R., & Santos, M. 1998b, *AJ*, 116, 1221
- Fabbiano, G., & Trinchieri, G. 1987, *ApJ*, 315, 46
- Fabbiano, G., & White, N. E. 2006, in Compact Stellar X-Ray Sources, ed. W. H. G. Lewin & M. van der Klis (Cambridge: Cambridge Univ. Press), 475
- Fabbiano, G. 2006, *ARA&A*, 44, 323
- Gehrels, N. 1986, *ApJ*, 303, 336
- Getman, K. V., et al. 2005, *ApJS*, 160, 319
- Giacconi, R., et al. 2001, *ApJ*, 551, 624
- Grimm, H.-J., McDowell, J., Zezas, A., Kim, D.-W., & Fabbiano, G. 2005, *ApJS*, 161, 271
- . 2007, *ApJS*, 173, 170
- Holt, S. S., Schlegel, E. M., Hwang, U., & Petre, R. 2003, *ApJ*, 588, 792
- Kalberla, P. M. W., Burton, W. B., Hartmann, D., Arnal, E. M., Bajaja, E., Morras, R., & Poeppel, W. G. L. 2005, *A&A*, 440, 775
- Karachentsev, I. D., Sharina, M. E., & Huchtmeier, W. K. 2000, *A&A*, 362, 544
- Kilgard, R. E., et al. 2005, *ApJS*, 159, 214
- Klein, U. 1983, *A&A*, 121, 150
- Kong, A. K. H., Garcia, M. R., Primini, F. A., Murray, S. S., Di Stefano, R., & McClintock, J. E. 2002, *ApJ*, 577, 738
- Kraft, R. P., Kregenow, J. M., Forman, W. R., Jones, C., & Murray, S. S. 2001, *ApJ*, 560, 675
- Kuulkers, E. 2004, *Nucl. Phys. B Proc. Suppl.*, 132, 466
- Lacey, C. K., & Duric, N. 2001, *ApJ*, 560, 719
- Larsen, S. S., Efremov, Y. N., Elmegreen, B. G., Alfaro, E. J., Battinelli, P., Hodge, P. W., & Richtler, T. 2002, *ApJ*, 567, 896
- Li, W. 2002, *IAU Circ.* 8005, <http://www.cfa.harvard.edu/iauc/08000/08005.html>
- Liu, J.-F., & Bregman, J. N. 2005, *ApJS*, 157, 59
- Liu, J.-F., Bregman, J. N., & Irwin, J. 2006, *ApJ*, 642, 171
- Matonick, D. M., & Fesen, R. A. 1997, *ApJS*, 112, 49
- Miller, M. C., & Colbert, E. J. M. 2004, *Int. J. Mod. Phys. D*, 13, 1
- Misra, K., Pooley, D., Chandra, P., Bhattacharya, D., Ray, A. K., Sagar, R., & Lewin, W. H. G. 2007, *MNRAS*, 381, 280
- Monet, D., et al. 1998, USNO-A V2.0, A Catalog of Astrometric Standards (Flagstaff: USNO)
- Nikiforov, I. I., Petrovskaya, I. V., & Ninkovic, S. 2000, in *IAU Colloq. 174, Small Galaxy Groups*, ed. M. J. Valtonen & C. Flynn (San Francisco: ASP), 399
- Prestwich, A. H., Irwin, J. A., Kilgard, R. E., Krauss, M. I., Zezas, A., Primini, F., Kaaret, P., & Boroson, B. 2003, *ApJ*, 595, 719
- Read, A. M., Ponman, T. J., & Strickland, D. K. 1997, *MNRAS*, 286, 626
- Rho, J., Jarrett, T. H., Chugai, N. N., & Chevalier, R. A. 2007, *ApJ*, 666, 1108
- Roberts, T. P., & Colbert, E. J. M. 2003, *MNRAS*, 341, L49
- Roberts, T. P., & Warwick, R. S. 2000, *MNRAS*, 315, 98
- Roberts, T. P., Warwick, R. S., Ward, M. J., & Murray, S. S. 2002, *MNRAS*, 337, 677
- Sauty, S., Gerin, M., & Casoli, F. 1998, *A&A*, 339, 19
- Schlegel, E. M. 1994a, *ApJ*, 424, L99
- . 1994b, *ApJ*, 434, 523
- . 1994c, *AJ*, 108, 1893
- Schlegel, E. M., Blair, W. P., & Fesen, R. A. 2000, *AJ*, 120, 791



- Schlegel, E. M., Holt, S. S., & Petre, R. 2003, *ApJ*, 598, 982
- Sharina, M. E., Karachentsev, I. D., & Tikhonov, N. A. 1997, *AstL*, 23, 373
- Sivakoff, G. R., Jordan, A., Juett, A. M., Sarazin, C. L., & Irwin, J. M. 2005a, in *IAU Symp. 230, Populations of High Energy Sources in Galaxies*, ed. E. J. A. Meurs & G. Fabbiano (Cambridge: Cambridge Univ. Press), 210
- Sivakoff, G. R., Sarazin, C. L., & Jordan, A. 2005b, *ApJ*, 624, L17
- Stark, A. A., Gammie, C. F., Wilson, R. W., Bally, J., Linke, R. A., Helles, C., & Hurwitz, M. 1992, *ApJS*, 79, 77
- Tacconi, L. J., & Young, J. S. 1986, *ApJ*, 308, 600
- Thronson, H. A., Jr., Hunter, D. A., Casey, S., Latter, W. B., & Harper, D. A. 1989, *ApJ*, 339, 803
- Townsley, L. K., Feigelson, E. D., Montmerle, T., Broos, P. S., Chu, Y.-H., & Garmire, G. P. 2003, *ApJ*, 593, 874
- Tully, R. B. 1988, *Catalog of Nearby Galaxies* (Cambridge: Cambridge Univ. Press)
- Vazquez, G. A., Hornschemeier, A. E., Colbert, E., Roberts, T. P., Ward, M. J., & Malhotra, S. 2007, *ApJ*, 658, L21
- Viallefond, F., Allen, R. J., & de Boer, J. A. 1980, *A&A*, 82, 207
- Zezas, A., Fabbiano, G., Baldi, A., Schweizer, F., King, A. R., Ponman, T. J., & Rots, A. H. 2006, *ApJS*, 166, 211
- Zezas, A., Fabbiano, G., Baldi, A., Schweizer, F., King, A. R., Rots, A. H., & Ponman, T. J. 2007, *ApJ*, 661, 135
- Zimmermann, U., Boese, G., Becker, W., Belloni, T., Doebereiner, S., Izzo, C., Kahabka, P., & Schwentker, O. 1998, *EXSAS User's Guide* (Garching: *ROSAT* Scientific Data Center), <http://www.mpe.mpg.de/xray/wave/rosat/doc/users-guide/exsasguide.php>

TABLE 9  
 BASIC *Chandra* SOURCE PROPERTIES FOR NGC 6946

No.	Source Designation CXOU J	Position (J2000.0)		S/N Ratio <sup>a</sup> ( $\sigma$ )	Photon Flux <sup>b</sup> ( $10^{-7}$ photons $s^{-1}$ $cm^{-2}$ )					Comb. <sup>c</sup>	Lum. <sup>d</sup> ( $10^{37}$ ergs $s^{-1}$ )		Comments <sup>g</sup>
		R. A.	Decl.		Obs. ID 1043	Obs. ID 4404	Obs. ID 4631	Obs. ID 4632	Obs. ID 4633		Avg. <sup>e</sup>	Max. <sup>f</sup>	
1	203419.0+601007	308.57942	60.16884	7.2	23.1 $\pm$ 3.3	9.7 $\pm$ 4.1	...	...	< 54.5	18.0 $\pm$ 2.4	2.2	2.5	
2	203421.4+601017	308.58923	60.17162	7.6	19.6 $\pm$ 3.5	36.3 $\pm$ 6.6	...	...	< 54.7	24.1 $\pm$ 3.0	5.5	8.1	
3	203423.4+601039	308.59770	60.17773	4.8	< 4.0	21.3 $\pm$ 4.7	...	...	29 $\pm$ 12	8.9 $\pm$ 1.7	1.1	3.4	T, N
4	203424.7+601038	308.60311	60.17737	7.9	30.5 $\pm$ 4.3	13.6 $\pm$ 4.2	...	...	41 $\pm$ 18	25.6 $\pm$ 3.1	6.6	8.4	
5	203425.0+600906	308.60426	60.15171	13.3	80.1 $\pm$ 6.1	< 8.5	...	...	19.9 $\pm$ 5.7	47.7 $\pm$ 3.5	7.1	12	T
6	203426.1+600909	308.60889	60.15262	32.1	343 $\pm$ 12	155 $\pm$ 12	...	...	127 $\pm$ 16	261.4 $\pm$ 8.0	32	44	
7	203426.2+600914	308.60940	60.15414	7.1	25.9 $\pm$ 4.1	17.1 $\pm$ 5.4	...	...	24 <sup>+15</sup> <sub>-10</sub>	23.2 $\pm$ 3.1	0.9	1.0	SSS
8	203429.1+601051	308.62137	60.18085	6.5	11.5 $\pm$ 2.4	28.4 $\pm$ 5.5	...	...	< 22.0	15.2 $\pm$ 2.2	2.2	4.8	T
9	203431.5+600638	308.63130	60.11069	3.1	7.5 $\pm$ 2.2	< 8.6	...	...	...	5.3 $\pm$ 1.5	1.1	1.6	
10	203431.5+601056	308.63156	60.18237	5.8	< 4.7	< 9.6	...	...	63 $\pm$ 11	10.2 $\pm$ 1.6	1.2	6.1	T, N
11	203432.0+601207	308.63347	60.20214	4.1	5.1 $\pm$ 1.8	9.7 $\pm$ 3.5	...	19.6 $\pm$ 9.6	< 17.1	7.6 $\pm$ 1.7	0.9	3.2	N
12	203432.4+600821	308.63541	60.13942	5.8	24.7 $\pm$ 3.7	< 5.0	...	...	< 5.1	12.0 $\pm$ 1.9	2.3	4.8	T
13	203434.4+601032	308.64362	60.17578	15.5	45.4 $\pm$ 4.7	47.0 $\pm$ 6.6	...	60 $\pm$ 11	84 $\pm$ 10	54.6 $\pm$ 3.4	4.7	7.0	S
14	203435.3+600742	308.64720	60.12853	4.6	8.0 $\pm$ 2.3	14.1 $\pm$ 4.4	...	...	< 15.3	9.0 $\pm$ 1.8	0.4	0.7	
15	203436.1+600839	308.65064	60.14428	7.8	18.6 $\pm$ 3.2	19.8 $\pm$ 5.0	...	< 35.6	27.3 $\pm$ 7.9	19.6 $\pm$ 2.4	1.1	1.2	LD
16	203436.4+600558	308.65168	60.09952	7.0	15.4 $\pm$ 2.9	26.8 $\pm$ 5.4	...	...	...	19.2 $\pm$ 2.6	4.2	5.7	
17	203436.5+600930	308.65220	60.15844	46.4	362 $\pm$ 13	581 $\pm$ 23	...	392 $\pm$ 21	416 $\pm$ 23	425.8 $\pm$ 9.1	31	42	
18	203437.2+600954	308.65533	60.16503	4.2	9.3 $\pm$ 2.6	7.2 $\pm$ 2.9	...	< 15.6	< 12.1	6.9 $\pm$ 1.5	1.8	2.5	
19	203437.2+601019	308.65535	60.17200	3.5	5.2 $\pm$ 1.7	4.0 <sup>+2.6</sup> <sub>-1.7</sub>	...	< 16.0	< 13.8	4.3 $\pm$ 1.1	0.5	0.6	
20	203437.9+600434	308.65798	60.07618	10.7	50.6 $\pm$ 7.5	59.8 $\pm$ 9.1	56 $\pm$ 10	...	...	55.7 $\pm$ 5.0	8.7	9.8	
21	203439.8+600822	308.66593	60.13967	8.4	22.9 $\pm$ 3.4	8.8 $\pm$ 3.3	7.7 <sup>+5.2</sup> <sub>-3.6</sub>	9.3 $\pm$ 4.1	15.7 $\pm$ 4.8	15.5 $\pm$ 1.8	3.3	4.7	
22	203440.5+600946	308.66916	60.16302	4.2	3.9 <sup>+2.1</sup> <sub>-1.5</sub>	< 8.4	10.3 <sup>+6.9</sup> <sub>-4.7</sub>	8.8 $\pm$ 4.1	9.1 $\pm$ 4.5	5.5 $\pm$ 1.2	1.0	1.9	N
23	203441.3+600846	308.67245	60.14620	5.1	5.1 $\pm$ 1.7	4.5 <sup>+3.2</sup> <sub>-2.1</sub>	11.8 $\pm$ 4.2	6.3 <sup>+4.6</sup> <sub>-3.1</sub>	7.4 <sup>+4.9</sup> <sub>-3.4</sub>	6.5 $\pm$ 1.2	0.9	1.7	LD
24	203442.0+600529	308.67535	60.09158	5.1	6.3 $\pm$ 1.8	13.3 $\pm$ 5.3	< 12.3	< 16.1	9.1 $\pm$ 3.7	6.6 $\pm$ 1.2	0.7	1.5	
25	203443.1+600652	308.67997	60.11457	4.1	7.3 $\pm$ 2.0	< 10.0	< 13.4	< 12.5	< 11.1	4.4 $\pm$ 1.0	0.9	1.6	
26	203443.2+600719	308.68432	60.12203	12.6	< 4.1	124 $\pm$ 11	22.5 $\pm$ 5.1	16.2 $\pm$ 4.2	16.6 $\pm$ 4.7	30.6 $\pm$ 2.3	6.6	29	SN 2002hh, T, N
27	203445.9+601049	308.69159	60.18035	5.8	13.0 $\pm$ 2.9	14.0 $\pm$ 5.0	8.7 $\pm$ 4.9	< 14.1	8.5 $\pm$ 4.4	10.6 $\pm$ 1.7	0.6	0.8	
28	203446.3+601328	308.69310	60.22451	10.9	27.2 $\pm$ 4.0	21.5 $\pm$ 5.0	31.8 $\pm$ 7.0	23.8 $\pm$ 6.2	36.9 $\pm$ 8.9	27.4 $\pm$ 2.4	5.3	6.8	
29	203447.1+600850	308.69626	60.14740	4.0	12.1 $\pm$ 2.5	< 5.4	< 6.6	< 7.1	< 5.2	4.0 $\pm$ 0.9	0.5	1.8	T
30	203447.5+601003	308.69803	60.16751	8.6	15.1 $\pm$ 3.0	10.1 $\pm$ 2.9	20.6 $\pm$ 5.5	19.0 $\pm$ 5.3	20.0 $\pm$ 6.3	16.3 $\pm$ 1.8	1.1	1.5	
31	203447.6+600932	308.69840	60.15905	13.0	6.3 $\pm$ 2.1	85.4 $\pm$ 8.7	6.3 <sup>+5.0</sup> <sub>-3.4</sub>	10.1 $\pm$ 4.1	60.7 $\pm$ 7.9	30.5 $\pm$ 2.3	3.4	9.3	
32	203448.4+600811	308.70193	60.13651	22.9	81.1 $\pm$ 5.9	71.3 $\pm$ 8.1	108 $\pm$ 10	39.8 $\pm$ 6.6	119 $\pm$ 12	83.2 $\pm$ 3.6	12	19	
33	203448.6+600941	308.70264	60.16155	4.4	12.8 $\pm$ 2.9	7.4 $\pm$ 2.8	< 10.4	< 5.5	< 10.3	4.9 $\pm$ 1.1	0.9	2.5	T
34	203448.8+600554	308.70341	60.09854	26.7	162.6 $\pm$ 9.3	163 $\pm$ 16	108 $\pm$ 12	133 $\pm$ 13	156 $\pm$ 14	148.2 $\pm$ 5.5	9.5	11	S
35	203449.0+601217	308.70445	60.20483	24.4	102.2 $\pm$ 6.9	114 $\pm$ 10	94 $\pm$ 10	73.6 $\pm$ 9.0	110 $\pm$ 11	99.9 $\pm$ 4.0	14	16	
36	203449.4+601342	308.70621	60.22846	5.6	13.0 $\pm$ 3.0	7.6 $\pm$ 3.1	13 <sup>+10</sup> <sub>-7.0</sub>	5.0 $\pm$ 3.1	6.5 $\pm$ 3.6	10.7 $\pm$ 1.8	1.9	2.6	
37	203449.7+601011	308.70717	60.16990	7.1	9.1 $\pm$ 2.2	11.0 $\pm$ 3.6	11.4 $\pm$ 3.9	13.8 $\pm$ 4.4	9.5 $\pm$ 4.2	10.7 $\pm$ 1.4	1.8	2.8	
38	203449.7+600806	308.70736	60.13504	4.6	6.7 $\pm$ 2.1	4.4 <sup>+3.2</sup> <sub>-2.0</sub>	< 9.9	9.1 <sup>+5.1</sup> <sub>-3.5</sub>	< 14.4	5.7 $\pm$ 1.1	0.4	0.7	LD
39	203449.7+601020	308.70745	60.17228	5.5	8.8 $\pm$ 2.2	3.9 <sup>+2.2</sup> <sub>-1.5</sub>	9.2 $\pm$ 3.6	5.2 $\pm$ 3.0	< 14.4	6.9 $\pm$ 1.2	1.1	2.2	
40	203450.0+600924	308.70851	60.15685	7.9	12.6 $\pm$ 2.7	16.3 $\pm$ 4.2	15.1 $\pm$ 5.7	13.6 $\pm$ 5.2	19.9 $\pm$ 5.7	15.1 $\pm$ 1.8	2.9	3.6	
41	203450.4+601016	308.71030	60.17112	5.1	7.9 $\pm$ 2.1	6.4 $\pm$ 2.6	9.2 $\pm$ 4.4	5.9 $\pm$ 3.3	< 11.2	6.5 $\pm$ 1.2	1.1	2.2	
42	203450.4+600724	308.71034	60.12337	13.5	< 2.3	50.7 $\pm$ 6.9	51.4 $\pm$ 7.3	47.0 $\pm$ 7.0	52.3 $\pm$ 8.6	31.8 $\pm$ 2.3	4.9	8.7	T, N
43	203450.7+600747	308.71149	60.12997	5.0	5.8 $\pm$ 1.8	4.9 <sup>+3.1</sup> <sub>-2.1</sub>	6.8 $\pm$ 2.9	4.3 <sup>+3.0</sup> <sub>-2.0</sub>	< 14.2	5.5 $\pm$ 1.0	0.4	0.6	
44	203450.7+601207	308.71165	60.20214	4.9	6.2 $\pm$ 1.9	8.2 $\pm$ 3.2	9.9 $\pm$ 4.2	2.9 $\pm$ 1.8	< 12.2	6.0 $\pm$ 1.2	1.0	2.4	
45	203450.9+601020	308.71215	60.17243	10.3	27.5 $\pm$ 4.0	18.0 $\pm$ 4.9	24.7 $\pm$ 5.9	18.7 $\pm$ 5.0	24.1 $\pm$ 7.0	23.6 $\pm$ 2.2	1.3	1.6	LD
46	203451.5+601248	308.71462	60.21335	5.4	5.1 $\pm$ 1.9	8.9 $\pm$ 3.3	10.0 $\pm$ 4.4	14.6 $\pm$ 5.4	6.2 $\pm$ 3.9	8.2 $\pm$ 1.4	1.5	2.5	
47	203451.5+600909	308.71470	60.15253	4.1	6.5 $\pm$ 2.4	4.7 <sup>+3.2</sup> <sub>-2.2</sub>	< 12.1	6.6 $\pm$ 3.5	7.6 $\pm$ 3.9	5.7 $\pm$ 1.3	0.4	0.7	MF, N
48	203453.3+601055	308.72237	60.18207	6.3	7.9 $\pm$ 2.2	11.3 $\pm$ 3.7	14.2 $\pm$ 4.9	6.2 $\pm$ 3.0	9.5 $\pm$ 4.2	9.5 $\pm$ 1.4	0.4	0.7	
49	203453.4+600719	308.72259	60.12208	8.5	5.4 $\pm$ 2.0	56.1 $\pm$ 7.9	< 10.6	8.9 $\pm$ 3.1	10.4 $\pm$ 3.8	14.9 $\pm$ 1.7	3.2	13	
50	203453.7+600910	308.72416	60.15286	7.2	9.6 $\pm$ 2.4	13.0 $\pm$ 4.2	14.2 $\pm$ 4.7	15.1 $\pm$ 4.8	9.1 $\pm$ 3.5	11.7 $\pm$ 1.5	1.8	2.2	N
51	203455.6+600930	308.73203	60.15856	7.4	2.6 $\pm$ 1.1	8.2 $\pm$ 2.8	6.7 $\pm$ 2.4	17.3 $\pm$ 4.3	21.2 $\pm$ 5.0	9.4 $\pm$ 1.2	1.2	2.7	
52	203456.5+600834	308.73547	60.14281	30.6	171.1 $\pm$ 9.1	116 $\pm$ 10	115 $\pm$ 10	163 $\pm$ 14	190 $\pm$ 14	153.1 $\pm$ 4.9	26	33	

TABLE 9 — *Continued*

No.	Source Designation CXOU J	Position (J2000.0)		S/N Ratio <sup>a</sup> ( $\sigma$ )	Photon Flux <sup>b</sup> ( $10^{-7}$ photons $s^{-1}$ $cm^{-2}$ )					Lum. <sup>d</sup> ( $10^{37}$ ergs $s^{-1}$ )		Comments <sup>g</sup>	
		R. A.	Decl.		Obs. ID 1043	Obs. ID 4404	Obs. ID 4631	Obs. ID 4632	Obs. ID 4633	Comb. <sup>c</sup>	Avg. <sup>e</sup>		Max. <sup>f</sup>
53	203456.5+600819	308.73562	60.13879	7.7	11.0 $\pm$ 2.5	16.3 $\pm$ 4.4	14.6 $\pm$ 4.1	8.2 <sup>+4.4</sup> <sub>-3.1</sub>	16.5 $\pm$ 5.5	13.0 $\pm$ 1.6	0.8	1.5	
54	203456.8+600532	308.73680	60.09235	10.1	22.7 $\pm$ 3.6	12.4 $\pm$ 4.2	17.3 $\pm$ 4.4	20.3 $\pm$ 4.8	30.0 $\pm$ 6.6	21.1 $\pm$ 2.0	3.0	4.3	
55	203456.9+601209	308.73725	60.20274	4.4	5.2 $\pm$ 2.1	11.1 $\pm$ 4.3	8.5 $\pm$ 4.2	5.7 <sup>+5.0</sup> <sub>-3.5</sub>	< 15.6	6.7 $\pm$ 1.4	0.9	1.5	S, N
56	203456.9+600826	308.73727	60.14064	6.4	< 6.7	3.7 <sup>+2.8</sup> <sub>-1.8</sub>	23.4 $\pm$ 5.3	< 13.6	18.0 $\pm$ 4.6	8.7 $\pm$ 1.3	1.2	3.8	N
57	203457.2+600733	308.73857	60.12598	3.3	3.7 <sup>+2.0</sup> <sub>-1.4</sub>	10.1 $\pm$ 4.0	< 10.0	< 5.4	< 7.9	3.4 $\pm$ 0.9	0.2	0.6	S, N
58	203457.7+600948	308.74058	60.16356	27.7	145.1 $\pm$ 7.7	83.8 $\pm$ 8.2	83.1 $\pm$ 8.7	80.4 $\pm$ 8.6	127 $\pm$ 11	111.2 $\pm$ 3.9	13	18	
59	203458.4+600934	308.74341	60.15954	9.3	15.9 $\pm$ 2.9	19.5 $\pm$ 4.4	11.8 $\pm$ 3.6	18.2 $\pm$ 4.6	12.9 $\pm$ 3.9	15.7 $\pm$ 1.6	1.9	2.4	SN 1968D
60	203500.1+600908	308.75057	60.15223	63.5	824 $\pm$ 19	791 $\pm$ 27	529 $\pm$ 24	477 $\pm$ 22	454 $\pm$ 23	664 $\pm$ 10	47	57	
61	203500.4+600859	308.75177	60.14976	6.0	3.7 $\pm$ 1.6	10.4 $\pm$ 4.2	14.6 $\pm$ 4.0	13.2 $\pm$ 4.2	< 13.0	8.2 $\pm$ 1.3	1.4	2.6	N
62	203500.6+601250	308.75257	60.21402	10.8	19.1 $\pm$ 3.2	29.4 $\pm$ 5.8	46.9 $\pm$ 7.9	17.8 $\pm$ 4.9	10.9 $\pm$ 4.1	24.0 $\pm$ 2.2	3.3	7.8	
63	203500.7+601130	308.75312	60.19183	145.3	3278 $\pm$ 36	2917 $\pm$ 49	2642 $\pm$ 49	3096 $\pm$ 53	3027 $\pm$ 54	3073 $\pm$ 21	310	330	ULX, LD, MF
64	203500.9+601010	308.75403	60.16972	33.0	165.0 $\pm$ 8.6	163 $\pm$ 12	214 $\pm$ 14	170 $\pm$ 13	161 $\pm$ 13	173.1 $\pm$ 5.2	26	32	
65	203501.1+600923	308.75482	60.15642	3.6	2.7 <sup>+1.8</sup> <sub>-1.3</sub>	6.1 <sup>+3.2</sup> <sub>-2.2</sub>	< 10.6	< 9.3	5.5 <sup>+3.8</sup> <sub>-2.5</sub>	3.3 $\pm$ 0.8	0.1	0.4	N
66	203501.9+601003	308.75818	60.16768	20.1	76.3 $\pm$ 6.2	60.7 $\pm$ 7.7	67.2 $\pm$ 8.1	52.6 $\pm$ 7.5	74.5 $\pm$ 9.0	68.0 $\pm$ 3.3	10	12	
67	203504.6+601117	308.76934	60.18821	11.6	24.1 $\pm$ 3.3	29.9 $\pm$ 5.5	15.8 $\pm$ 4.6	24.6 $\pm$ 5.8	27.4 $\pm$ 5.7	24.3 $\pm$ 2.0	1.8	2.4	
68	203504.6+600918	308.76952	60.15512	5.4	8.4 $\pm$ 2.4	9.3 $\pm$ 3.5	< 13.8	5.1 <sup>+3.3</sup> <sub>-2.2</sub>	5.8 <sup>+3.3</sup> <sub>-2.3</sub>	7.2 $\pm$ 1.2	0.5	0.6	
69	203505.3+600623	308.77223	60.10640	15.8	46.3 $\pm$ 4.9	38.8 $\pm$ 6.8	41.3 $\pm$ 6.3	46.4 $\pm$ 7.0	39.6 $\pm$ 6.4	43.4 $\pm$ 2.7	7.1	7.9	
70	203505.5+600742	308.77306	60.12843	4.8	3.4 $\pm$ 1.6	< 16.7	9.0 $\pm$ 3.6	7.4 <sup>+4.2</sup> <sub>-2.8</sub>	7.3 <sup>+3.7</sup> <sub>-2.6</sub>	5.8 $\pm$ 1.1	1.0	1.6	N
71	203506.5+601040	308.77742	60.17781	9.1	12.9 $\pm$ 2.8	13.3 $\pm$ 3.6	13.3 $\pm$ 4.2	15.6 $\pm$ 4.5	31.4 $\pm$ 6.3	16.3 $\pm$ 1.7	3.0	6.1	
72	203508.1+601113	308.78403	60.18696	7.4	9.8 $\pm$ 2.6	20.3 $\pm$ 5.0	13.4 $\pm$ 4.7	10.3 $\pm$ 4.0	13.0 $\pm$ 4.4	12.7 $\pm$ 1.6	1.2	1.7	LD
73	203510.1+601000	308.79234	60.16692	5.0	7.9 $\pm$ 2.6	< 12.6	5.2 <sup>+3.2</sup> <sub>-2.2</sub>	6.9 $\pm$ 2.9	5.2 <sup>+3.3</sup> <sub>-2.3</sub>	6.2 $\pm$ 1.1	1.0	1.3	N
74	203510.9+600856	308.79543	60.14912	5.2	6.8 $\pm$ 2.4	7.1 <sup>+3.8</sup> <sub>-2.7</sub>	5.4 <sup>+2.9</sup> <sub>-2.0</sub>	11.0 $\pm$ 4.5	5.6 <sup>+3.7</sup> <sub>-2.4</sub>	7.1 $\pm$ 1.3	0.3	0.6	N
75	203512.5+600837	308.80213	60.14377	3.7	3.2 $\pm$ 2.0	< 11.3	5.0 <sup>+3.7</sup> <sub>-2.3</sub>	5.4 <sup>+3.5</sup> <sub>-2.3</sub>	4.7 <sup>+3.4</sup> <sub>-2.2</sub>	4.1 $\pm$ 1.0	0.7	1.1	N
76	203512.7+600731	308.80321	60.12551	22.5	84.2 $\pm$ 6.4	61.0 $\pm$ 8.7	73.1 $\pm$ 8.2	106 $\pm$ 11	110 $\pm$ 11	86.8 $\pm$ 3.8	12	17	
77	203513.1+600907	308.80461	60.15207	4.4	4.1 $\pm$ 2.1	11.3 $\pm$ 3.7	< 15.2	< 12.8	4.9 <sup>+3.2</sup> <sub>-2.1</sub>	5.6 $\pm$ 1.2	1.3	2.3	N
78	203513.6+600522	308.80690	60.08950	6.6	...	26.0 $\pm$ 6.4	10.6 $\pm$ 3.1	14.8 $\pm$ 4.2	4.5 <sup>+2.8</sup> <sub>-1.8</sub>	13.2 $\pm$ 1.9	1.8	3.8	N
79	203516.2+601046	308.81773	60.17959	16.0	29.2 $\pm$ 4.5	159 $\pm$ 14	80.7 $\pm$ 9.2	< 10.1	10.0 $\pm$ 3.8	51.0 $\pm$ 3.1	8.0	23	T
80	203517.3+600813	308.82214	60.13719	4.7	4.8 $\pm$ 2.1	16 <sup>+11</sup> <sub>-7.0</sub>	6.6 <sup>+3.4</sup> <sub>-2.4</sub>	6.6 <sup>+3.3</sup> <sub>-2.3</sub>	3.3 <sup>+2.3</sup> <sub>-1.5</sub>	5.8 $\pm$ 1.1	1.0	1.8	N
81	203518.7+601056	308.82830	60.18237	30.7	173.8 $\pm$ 8.7	109 $\pm$ 10	104.3 $\pm$ 9.4	136 $\pm$ 11	132 $\pm$ 11	138.1 $\pm$ 4.4	19	24	
82	203520.0+600933	308.83336	60.15940	4.8	11.2 $\pm$ 3.0	< 10.3	10.4 $\pm$ 4.0	< 9.2	< 13.2	6.9 $\pm$ 1.3	0.5	1.0	
83	203521.1+600951	308.83813	60.16437	6.0	8.6 $\pm$ 2.8	8.6 $\pm$ 3.7	12.7 $\pm$ 4.1	12.7 $\pm$ 4.3	5.8 <sup>+4.0</sup> <sub>-2.6</sub>	9.5 $\pm$ 1.5	0.8	1.1	
84	203525.3+600717	308.85565	60.12156	21.7	...	< 11.5	183 $\pm$ 13	152 $\pm$ 13	150 $\pm$ 13	128.5 $\pm$ 5.8	19	30	SN 2004et, T, N
85	203525.5+600958	308.85651	60.16629	12.4	38.8 $\pm$ 5.0	39.6 $\pm$ 9.7	31.6 $\pm$ 5.8	22.0 $\pm$ 5.1	37.1 $\pm$ 7.0	34.1 $\pm$ 2.7	2.9	3.8	
86	203527.8+600920	308.86604	60.15559	9.3	21.7 $\pm$ 3.7	22.0 $\pm$ 7.3	16.4 $\pm$ 4.2	18.4 $\pm$ 4.8	17.3 $\pm$ 4.8	19.4 $\pm$ 2.0	3.2	3.7	
87	203528.6+600605	308.86937	60.10157	3.8	...	3.9 <sup>+2.8</sup> <sub>-1.8</sub>	5.6 <sup>+3.2</sup> <sub>-2.1</sub>	7.5 $\pm$ 3.0	< 13.6	5.1 $\pm$ 1.2	0.7	1.1	N
88	203530.1+600623	308.87569	60.10648	11.7	...	51 $\pm$ 10	47.5 $\pm$ 7.2	43.3 $\pm$ 7.2	42.7 $\pm$ 7.4	45.6 $\pm$ 3.7	3.0	3.4	SN 1980K, N
89	203530.6+600737	308.87770	60.12714	6.4	...	18.6 <sup>+11</sup> <sub>-7.6</sub>	18.0 $\pm$ 5.2	21.4 $\pm$ 6.1	23.6 $\pm$ 6.3	20.4 $\pm$ 3.0	1.0	1.1	S, N
90	203532.2+601018	308.88442	60.17180	8.9	25.8 $\pm$ 5.7	...	21.3 $\pm$ 4.5	27.8 $\pm$ 6.1	19.5 $\pm$ 4.9	23.9 $\pm$ 2.6	3.8	5.2	N

<sup>a</sup> Photometric signal-to-noise ratio based on all observations, as computed by ACIS Extract.<sup>b</sup> Background-subtracted photon fluxes in the full 0.3 – 7 keV band. For sources with fewer than five net counts in an observation an upper limit with 3  $\sigma$  Gaussian confidence is given.<sup>c</sup> Photon flux in the co-added exposure.<sup>d</sup> X-ray luminosity in the 0.3 – 7 keV band.<sup>e</sup> Luminosity calculated from a co-added exposure spanning all the observations.<sup>f</sup> Luminosity calculated from the observation in which the source is brightest.<sup>g</sup> (T) transient candidate; (N) source not detected by Holt et al. (2003); (SSS) supersoft source candidate; (S) source is most likely a foreground star; (LD) source coincides with a supernova remnant in the list of Lacey & Duric (2001); (MF) source coincides with a supernova remnant in the list of Matonick & Fesen (1997).

TABLE 10  
 BASIC *Chandra* SOURCE PROPERTIES FOR NGC 4485/4490

No.	Source Designation CXOU J	Position (J2000.0)		S/N Ratio <sup>a</sup> ( $\sigma$ )	Photon Flux <sup>b</sup> ( $10^{-7}$ photons $s^{-1}$ $cm^{-2}$ )				Lum. <sup>d</sup> ( $10^{37}$ ergs $s^{-1}$ )		Comments <sup>g</sup>
		R. A.	Decl.		Obs. ID	Obs. ID	Obs. ID	Comb. <sup>c</sup>	Avg. <sup>e</sup>	Max. <sup>f</sup>	
					1579	4725	4726				
1	123025.2+413924	187.60506	41.65691	15.6	73 ± 10	70.5 ± 7.5	77.5 ± 7.5	73.9 ± 4.6	22	23	
2	123026.7+413821	187.61165	41.63942	5.2	< 9.4	15.0 ± 3.7	10.2 ± 2.8	9.8 ± 1.8	2.2	3.3	T, N
3	123027.1+413814	187.61330	41.63724	8.7	25.1 ± 6.5	27.0 ± 4.8	25.1 ± 4.5	25.7 ± 2.8	9.3	10	
4	123027.6+413941	187.61528	41.66161	4.1	< 17.9	2.8 <sup>+1.9</sup> <sub>-1.3</sub>	12.4 ± 3.3	6.7 ± 1.5	1.5	2.8	N
5	123028.2+413958	187.61779	41.66622	4.2	18.4 ± 5.3	6.6 ± 2.9	< 12.7	7.4 ± 1.6	1.3	3.2	
6	123028.5+413926	187.61913	41.65731	5.6	19.7 ± 5.9	11.5 ± 3.3	10.5 ± 3.3	12.8 ± 2.1	5.3	8.0	
7	123028.7+413757	187.61969	41.63254	9.5	12.1 ± 4.3	20.1 ± 4.4	58.9 ± 7.3	33.7 ± 3.4	9.8	17	
8	123029.0+414046	187.62122	41.67961	6.9	19.4 ± 5.7	20.8 ± 4.3	13.1 ± 3.4	17.4 ± 2.4	3.7	4.8	
9	123029.4+413927	187.62278	41.65771	31.6	316 ± 20	302 ± 14	209 ± 12	265.1 ± 8.2	100	117	ULX-1
10	123029.4+414058	187.62281	41.68293	3.3	< 18.1	8.1 ± 3.3	5.2 <sup>+3.0</sup> <sub>-2.0</sub>	5.8 ± 1.6	0.8	1.4	N
11	123030.3+413853	187.62630	41.64811	22.5	186 ± 16	230 ± 13	49.8 ± 6.7	154.7 ± 6.7	43	64	
12	123030.3+414126	187.62662	41.69067	6.2	< 8.9	14.7 ± 3.7	20.5 ± 3.9	13.7 ± 2.1	3.6	5.8	T, N
13	123030.4+414142	187.62698	41.69509	67.8	1557 ± 42	1071 ± 26	975 ± 25	1115 ± 16	280	410	ULX-2
14	123030.7+413911	187.62807	41.65326	55.8	776 ± 31	855 ± 25	785 ± 22	821 ± 15	288	295	ULX-3
15	123031.0+413837	187.62937	41.64376	5.6	15.6 ± 5.1	6.7 ± 2.3	15.0 ± 3.8	11.8 ± 2.0	4.5	6.8	
16	123031.3+413901	187.63048	41.65053	6.4	14.8 ± 5.0	9.3 ± 3.6	22.7 ± 4.3	16.2 ± 2.4	4.0	5.3	
17	123031.6+414140	187.63184	41.69471	28.2	< 12.3	193 ± 12	400 ± 17	233.1 ± 8.1	48	83	T, N
18	123032.1+413918	187.63411	41.65508	56.8	602 ± 27	1078 ± 30	844 ± 22	870 ± 15	282	347	ULX-4
19	123032.8+413845	187.63667	41.64587	4.0	< 22.8	4.3 ± 1.9	10.4 ± 3.2	6.7 ± 1.5	1.0	1.7	N
20	123032.9+414014	187.63719	41.67064	6.8	8.5 <sup>+4.8</sup> <sub>-3.3</sub>	21.9 ± 4.4	17.0 ± 3.9	17.2 ± 2.4	6.3	7.6	N
21	123034.1+413859	187.64218	41.64984	5.2	< 11.9	12.6 ± 3.3	12.3 ± 3.2	9.9 ± 1.8	3.4	4.7	N
22	123034.2+413805	187.64263	41.63484	6.5	26.9 ± 6.3	16.7 ± 3.9	9.7 ± 3.3	16.4 ± 2.3	6.4	8.5	
23	123034.3+413850	187.64320	41.64724	19.1	155 ± 14	61.8 ± 6.7	119.4 ± 9.4	104.3 ± 5.3	25	39	
24	123034.5+413834	187.64377	41.64290	4.3	7.5 <sup>+5.2</sup> <sub>-3.4</sub>	12.5 ± 4.4	12.3 ± 4.2	11.3 ± 2.4	0.9	1.2	SSS, N
25	123035.1+413846	187.64648	41.64638	31.7	34.1 ± 6.9	241 ± 12	362 ± 15	240.8 ± 7.5	67	103	ULX-5
26	123035.8+413832	187.64926	41.64247	6.0	12.7 ± 4.5	19.0 ± 4.4	10.7 ± 3.1	14.2 ± 2.2	3.4	5.2	
27	123036.2+413837	187.65101	41.64388	47.2	607 ± 27	176 ± 10	794 ± 21	516 ± 11	154	229	ULX-6
28	123037.7+413823	187.65748	41.63991	3.9	8.2 <sup>+5.3</sup> <sub>-3.5</sub>	7.7 ± 2.9	4.9 ± 2.0	6.7 ± 1.6	2.2	3.4	N
29	123038.2+413831	187.65926	41.64198	5.0	12.3 ± 4.5	18.0 ± 5.1	6.2 ± 2.4	11.4 ± 2.1	1.6	2.4	
30	123038.4+413831	187.66012	41.64218	27.4	< 9.1	< 7.9	444 ± 16	187.5 ± 6.7	59	139	ULX-7, T, N
31	123038.4+413743	187.66026	41.62863	12.2	63.6 ± 9.6	48.8 ± 6.3	47.4 ± 6.9	52.1 ± 4.1	9.1	11	
32	123038.8+413810	187.66207	41.63614	17.1	54.2 ± 8.2	51.2 ± 6.0	123.8 ± 9.2	81.4 ± 4.6	28	45	
33	123040.3+413813	187.66806	41.63714	22.1	127 ± 13	120.8 ± 9.1	149 ± 10	134.0 ± 5.9	40	48	
34	123043.0+413756	187.67928	41.63248	5.7	14.4 ± 4.5	9.8 ± 3.3	11.6 ± 3.0	11.5 ± 1.9	1.4	1.8	
35	123043.1+413818	187.67985	41.63854	63.7	1052 ± 35	770 ± 21	1036 ± 24	929 ± 14	279	332	ULX-8
36	123045.5+413640	187.68984	41.61114	9.3	24.0 ± 5.9	33.2 ± 5.0	23.1 ± 4.3	27.6 ± 2.8	7.1	9.8	
37	123047.7+413807	187.69894	41.63547	5.0	13.2 ± 4.9	7.9 ± 2.6	7.9 ± 2.5	9.1 ± 1.7	2.3	3.5	
38	123047.7+413727	187.69906	41.62433	7.6	46.9 ± 8.7	16.1 ± 3.9	11.9 ± 3.3	21.7 ± 2.7	5.0	9.0	

<sup>a</sup> Photometric signal-to-noise ratio based on all observations, as computed by ACIS Extract.

<sup>b</sup> Background-subtracted photon fluxes in the full 0.3 – 7 keV band. For sources with fewer than five net counts in an observation an upper limit with 3  $\sigma$  Gaussian confidence is given.

<sup>c</sup> Photon flux in the co-added exposure.

<sup>d</sup> Observed X-ray luminosity in the 0.3 – 7 keV band.

<sup>e</sup> Luminosity calculated from a co-added exposure spanning all the observations.

<sup>f</sup> Luminosity calculated from the observation in which the source is brightest.

<sup>g</sup> (T) transient candidate; (N) source not detected by Roberts et al. (2002); (SSS) supersoft source candidate.

TABLE 11  
*Chandra* VARIABILITY PROPERTIES FOR NGC 6946 SOURCES

No.	Source Designation CXOU J	K-S Test for Short-Term Flux Variability <sup>a</sup>					Long-Term Variability				Comments <sup>f</sup>
		Obs. ID	Obs. ID	Obs. ID	Obs. ID	Obs. ID	Flux		Hardness Ratios		
		1043	4404	4631	4632	4633	$S_{\text{flux}}^b$	$R^c$	$S_{\text{HR1}}^d$	$S_{\text{HR2}}^e$	
1	203419.0+601007	0.12	0.94	...	...	0.83	2.2	2.4	0.5	0.8	
2	203421.4+601017	0.96	0.98	...	...	0.39	2.0	3.9	0.6	0.2	
3	203423.4+601039	...	0.66	...	...	0.13	4.0	110	0.7	0.5	1
4	203424.7+601038	0.65	0.68	...	...	0.29	2.5	3.0	0.9	1.4	
5	203425.0+600906	0.30	...	...	...	0.15	11.9	73.0	0.8	0.5	1
6	203426.1+600909	0.48	0.69	...	...	0.77	10.9	2.7	0.6	1.6	1
7	203426.2+600914	0.58	0.47	...	...	0.49	1.2	1.5	0.4	0.3	
8	203429.1+601051	0.33	0.85	...	...	...	3.2	> 1.5	0.5	0.9	1
9	203431.5+600638	0.25	...	...	...	...	1.9	7.1	0.4	0.3	
10	203431.5+601056	...	...	...	...	0.46	5.5	78.3	0.3	0.7	1
11	203432.0+601207	0.15	0.39	...	0.33	...	1.6	> 1.4	1.6	1.7	
12	203432.4+600821	0.79	...	...	...	...	6.0	> 5.0	0.0	0.0	1
13	203434.4+601032	0.03	0.65	...	0.82	0.13	3.3	1.8	1.5	0.9	1, star
14	203435.3+600742	0.22	0.44	...	...	0.17	1.7	4.0	0.3	0.3	
15	203436.1+600839	0.67	0.74	...	0.23	0.55	1.6	3.5	1.1	0.7	
16	203436.4+600558	0.30	0.41	...	...	...	1.7	1.7	0.4	0.4	
17	203436.5+600930	0.21	0.69	...	0.93	0.85	8.2	1.6	3.5	1.7	1, sp
18	203437.2+600954	0.02	0.92	...	0.16	0.90	1.8	6.8	1.1	1.0	
19	203437.2+601019	0.97	0.45	...	0.75	0.57	0.7	2.3	1.1	1.0	
20	203437.9+600434	0.42	0.46	0.18	...	...	0.7	1.2	0.9	1.3	
21	203439.8+600822	0.86	0.95	0.81	0.43	0.11	2.6	3.0	1.3	1.1	
22	203440.5+600946	0.18	...	0.82	0.87	0.91	1.4	7.9	1.0	1.1	
23	203441.3+600846	0.22	0.44	0.15	0.44	0.58	1.3	2.6	0.8	0.5	
24	203442.0+600529	0.07	0.35	0.37	...	0.29	1.5	4.8	1.2	1.4	
25	203443.1+600652	0.34	...	0.91	0.13	...	1.7	7.2	0.3	0.6	
26	203444.2+600719	...	0.29	0.92	0.60	0.44	10.2	225	0.6	3.5	1, sp
27	203445.9+601049	0.01	0.39	0.88	0.16	0.97	2.1	5.0	0.5	0.8	
28	203446.3+601328	0.36	0.02	0.13	0.15	0.80	1.4	1.7	1.4	1.5	
29	203447.1+600850	0.65	...	...	...	...	4.0	> 2.3	0.0	0.0	1
30	203447.5+601003	0.61	0.97	0.20	0.73	0.29	1.5	2.0	2.3	1.1	
31	203447.6+600932	0.95	0.58	0.31	0.90	0.42	8.4	13.6	1.6	1.2	1
32	203448.4+600811	0.01	0.72	0.30	0.10	0.30	5.7	3.0	1.4	1.7	1
33	203448.6+600941	0.81	0.99	0.75	...	0.44	3.8	> 2.3	0.4	0.7	1
34	203448.8+600554	0.18	$2.4 \times 10^{-3}$	0.75	0.01	0.07	3.5	1.5	1.2	1.5	s, 1, star
35	203449.0+601217	0.85	0.33	0.47	0.50	0.50	2.8	1.5	1.9	1.8	
36	203449.4+601342	0.80	0.23	0.57	$2.2 \times 10^{-3}$	0.32	1.7	2.6	1.4	0.9	s
37	203449.7+601011	0.46	0.54	0.66	0.37	0.12	0.9	1.5	1.0	1.2	
38	203449.7+600806	0.26	0.30	...	0.83	0.28	1.5	5.2	0.7	0.6	
39	203449.7+601020	0.95	0.92	0.64	0.09	0.07	1.5	2.8	0.9	1.6	
40	203450.0+600924	0.43	0.34	0.34	0.87	0.33	1.0	1.6	1.3	1.1	
41	203450.4+601016	0.95	0.96	0.10	$2.4 \times 10^{-3}$	...	1.8	8.5	0.4	1.0	s
42	203450.4+600724	...	0.82	0.34	0.40	0.99	6.9	> 22.7	1.1	1.6	1
43	203450.7+600747	0.69	0.04	0.22	0.23	0.15	0.6	1.8	0.4	0.6	
44	203450.7+601207	0.70	0.21	$4.6 \times 10^{-3}$	0.84	0.90	1.5	8.5	0.7	1.1	
45	203450.9+601020	0.65	0.05	0.12	0.83	0.61	1.4	1.5	1.1	1.5	
46	203451.5+601248	0.13	0.36	0.98	0.72	0.31	1.5	2.9	1.0	1.1	
47	203451.5+600909	0.13	0.81	0.12	0.89	0.77	1.3	12.3	0.6	1.1	
48	203453.3+601055	0.50	0.15	0.19	0.63	0.15	1.2	2.3	1.3	1.1	
49	203453.4+600719	0.55	0.26	...	0.20	0.59	6.1	25.8	0.8	1.5	1
50	203453.7+600910	0.07	0.59	0.78	0.93	0.30	0.9	1.7	1.5	0.5	
51	203455.6+600930	0.30	0.28	0.41	0.34	0.11	3.2	8.2	1.4	0.8	1
52	203456.5+600834	0.01	1.00	0.82	0.50	0.06	4.2	1.7	1.6	0.8	1
53	203456.5+600819	0.01	0.57	0.83	0.70	0.38	1.2	2.0	1.5	1.0	
54	203456.8+600532	0.77	0.87	0.81	0.01	0.62	2.0	2.4	1.6	0.7	
55	203456.9+601209	0.37	0.25	0.60	0.23	0.16	1.2	3.1	1.1	0.7	star
56	203456.9+600826	0.08	0.08	0.69	0.46	0.02	3.6	12.8	0.4	1.0	1
57	203457.2+600733	0.70	0.06	...	...	...	2.1	> 1.9	1.0	1.0	star
58	203457.7+600948	0.35	0.10	0.40	0.88	0.08	5.4	1.8	1.2	1.0	1
59	203458.4+600934	0.19	0.64	0.01	0.53	0.83	1.2	1.6	0.5	1.5	
60	203500.1+600908	$6.2 \times 10^{-15}$	0.24	0.50	0.76	0.80	12.2	1.8	1.2	0.9	s, 1
61	203500.4+600859	0.18	0.77	0.34	0.37	0.48	2.2	4.6	0.8	1.1	
62	203500.6+601250	0.08	0.58	0.80	0.77	0.95	3.7	4.3	1.3	0.8	1
63	203500.7+601130	0.48	0.67	0.25	0.31	0.61	8.9	1.2	2.9	1.8	1
64	203500.9+601010	0.86	0.40	0.11	0.54	0.64	2.9	1.3	0.7	2.1	
65	203501.1+600923	0.96	0.34	...	...	0.76	1.2	4.7	0.8	0.5	
66	203501.9+601003	0.98	0.04	0.26	0.13	0.96	2.3	1.5	0.7	1.9	
67	203504.6+601117	0.48	0.59	0.81	0.84	0.36	1.8	1.9	1.4	0.6	
68	203504.6+600918	0.26	0.69	0.26	0.63	0.43	1.1	2.3	1.0	0.9	
69	203505.3+600623	0.12	0.22	0.57	0.51	0.91	0.8	1.2	1.5	1.6	
70	203505.5+600742	0.73	...	0.20	0.36	0.58	1.2	2.6	1.2	0.6	
71	203506.5+601040	0.28	0.41	0.02	0.85	0.20	2.5	2.4	1.3	1.7	
72	203508.1+601113	0.68	0.76	0.96	0.35	0.89	1.7	2.1	1.6	1.0	

TABLE 11 — *Continued*

No.	Source Designation CXOU J	K-S Test for Short-Term Flux Variability <sup>a</sup>					Long-Term Variability				Comments <sup>f</sup>
		Obs. ID	Obs. ID	Obs. ID	Obs. ID	Obs. ID	Flux		Hardness Ratios		
		1043	4404	4631	4632	4633	$S_{\text{flux}}^b$	$R^c$	$S_{\text{HR1}}^d$	$S_{\text{HR2}}^e$	
73	203510.1+601000	0.47	0.33	0.70	0.34	0.58	1.1	2.2	1.2	0.8	
74	203510.9+600856	0.48	0.18	0.57	0.40	0.39	0.9	2.0	1.7	0.8	
75	203512.5+600837	0.02	0.38	0.46	0.90	0.22	0.6	1.9	0.7	0.9	
76	203512.7+600731	0.63	0.71	0.71	0.06	0.74	3.3	1.8	1.7	0.9	l
77	203513.1+600907	0.46	0.21	0.47	...	0.16	1.6	4.4	1.3	1.2	
78	203513.6+600522	...	0.96	0.52	0.94	0.19	2.8	5.8	0.9	0.7	
79	203516.2+601046	$4.9 \times 10^{-16}$	0.80	0.19	...	0.06	10.9	118	1.5	2.3	s, l
80	203517.3+600813	0.40	0.09	0.37	0.72	0.30	1.1	4.8	1.1	0.9	
81	203518.7+601056	0.51	0.98	0.47	0.95	0.53	5.2	1.7	1.3	1.6	l
82	203520.0+600933	0.51	...	0.76	...	0.84	2.4	9.2	0.4	1.2	
83	203521.1+600951	0.42	0.88	0.90	0.52	0.28	1.1	2.2	0.5	0.9	
84	203525.3+600717	...	...	0.41	0.12	0.76	12.9	112	0.6	2.2	l
85	203525.5+600958	0.92	0.98	0.07	0.30	0.96	2.2	1.8	1.0	1.2	
86	203527.8+600920	0.34	0.66	0.63	0.63	1.00	0.9	1.3	0.7	1.0	
87	203528.6+600605	...	0.08	0.63	0.14	...	0.9	2.4	0.9	1.0	
88	203530.1+600623	...	0.85	0.22	0.65	0.39	0.6	1.2	0.6	1.0	
89	203530.6+600737	...	0.07	0.82	0.02	0.67	0.6	1.3	0.8	0.6	star
90	203532.2+601018	0.10	...	0.31	0.24	0.01	0.9	1.4	1.8	1.7	

<sup>a</sup> Significance level of a one-sided Kolmogorov-Smirnov test statistic with respect to a uniform count-rate model.

$$^b S_{\text{flux}} = \max_{i,j} |F_i - F_j| / \sqrt{\sigma_{F_i}^2 + \sigma_{F_j}^2}$$

<sup>c</sup>  $R = F_{\text{max}}/F_{\text{min}}$ . For sources with no detected flux in at least one of the observations a lower limit with  $3\sigma$  Gaussian confidence is given.

$$^d S_{\text{HR1}} = \max_{i,j} |\text{HR1}_i - \text{HR1}_j| / \sqrt{\sigma_{\text{HR1},i}^2 + \sigma_{\text{HR1},j}^2}$$

$$^e S_{\text{HR2}} = \max_{i,j} |\text{HR2}_i - \text{HR2}_j| / \sqrt{\sigma_{\text{HR2},i}^2 + \sigma_{\text{HR2},j}^2}$$

<sup>f</sup> Short-term flux variability is denoted by “s,” long-term flux variability by “l,” and spectral variability by “sp.” Foreground stars are indicated by “star.”

TABLE 12  
*Chandra* VARIABILITY PROPERTIES FOR NGC 4485/4490 SOURCES

No.	Source Designation CXOU J	K-S Test for Short-Term Flux Variability <sup>a</sup>			Long-Term Variability				Comments <sup>f</sup>
		Obs. ID	Obs. ID	Obs. ID	Flux		Hardness Ratios		
		1579	4725	4726	$S_{\text{flux}}^b$	$R^c$	$S_{\text{HR1}}^d$	$S_{\text{HR2}}^e$	
1	123025.2+413924	0.35	0.50	0.61	0.6	1.1	1.1	1.8	
2	123026.7+413821	...	0.25	1.00	3.1	> 1.6	1.2	1.6	l
3	123027.1+413814	0.84	0.72	0.35	0.3	1.1	0.5	1.3	
4	123027.6+413941	...	0.35	0.77	2.3	4.5	0.8	0.8	
5	123028.2+413958	0.10	0.73	0.42	2.3	5.4	1.3	0.5	
6	123028.5+413926	0.82	0.05	0.94	1.2	1.9	1.3	0.8	
7	123028.7+413757	0.87	0.84	0.90	5.1	4.9	1.3	2.0	l
8	123029.0+414046	0.22	0.62	0.57	1.3	1.6	0.5	0.3	
9	123029.4+413927	0.84	0.89	0.68	5.4	1.5	1.0	0.4	l
10	123029.4+414058	...	0.55	0.80	0.7	2.0	0.6	1.2	
11	123030.3+413853	$1.2 \times 10^{-4}$	$4.0 \times 10^{-5}$	0.18	12.0	4.6	1.3	1.8	s, l
12	123030.3+414126	...	0.83	0.88	4.2	> 2.3	1.3	1.2	l
13	123030.4+414142	0.60	0.50	0.94	12.1	1.6	2.1	2.6	l
14	123030.7+413911	0.46	0.84	0.40	2.1	1.1	0.6	0.4	
15	123031.0+413837	0.31	0.11	0.06	1.6	2.3	0.5	1.4	
16	123031.3+413901	0.60	0.92	0.93	2.1	2.4	0.8	0.8	
17	123031.6+414140	...	0.30	0.14	22.8	721	0.2	1.8	l
18	123032.1+413918	0.66	0.76	0.50	11.9	1.8	1.2	1.9	l
19	123032.8+413845	0.15	0.60	0.24	1.4	2.4	0.9	0.7	
20	123032.9+414014	0.30	0.51	0.74	2.0	2.6	0.8	0.6	
21	123034.1+413859	...	0.24	0.84	2.5	30.4	0.8	0.2	
22	123034.2+413805	0.62	0.13	0.72	2.2	2.8	0.8	1.0	
23	123034.3+413850	0.82	0.49	$2.6 \times 10^{-4}$	5.7	2.5	2.2	3.5	s, l, sp
24	123034.5+413834	0.03	0.79	0.77	0.7	1.7	0.5	0.7	
25	123035.1+413846	0.34	$3.9 \times 10^{-11}$	0.57	19.5	10.6	1.6	1.1	s, l
26	123035.8+413832	0.64	0.44	0.95	1.4	1.8	1.5	2.4	
27	123036.2+413837	0.82	0.06	0.22	26.0	4.5	0.9	4.0	l, sp
28	123037.7+413823	0.38	0.74	0.68	0.7	1.7	0.7	1.3	
29	123038.2+413831	0.81	0.45	0.19	1.8	2.9	1.2	0.9	
30	123038.4+413831	...	...	0.87	27.2	> 60.4	0.2	0.2	l
31	123038.4+413743	0.43	0.67	0.83	1.3	1.3	1.1	0.7	
32	123038.8+413810	$9.6 \times 10^{-4}$	0.03	$9.4 \times 10^{-15}$	6.3	2.4	1.2	2.3	s, l
33	123040.3+413813	0.21	0.27	0.39	2.0	1.2	1.1	0.5	
34	123043.0+413756	0.75	0.67	0.30	0.7	1.5	1.2	0.5	
35	123043.1+413818	0.51	0.47	0.31	8.1	1.4	1.0	3.6	l, sp
36	123045.5+413640	0.52	0.13	0.34	1.4	1.4	1.1	1.4	
37	123047.7+413807	0.21	0.36	0.21	0.8	1.7	1.0	0.7	
38	123047.7+413727	0.88	0.27	0.85	3.4	3.9	0.9	0.7	l

<sup>a</sup> Significance level of a one-sided Kolmogorov-Smirnov test statistic with respect to a uniform count-rate model.

$$^b S_{\text{flux}} = \max_{i,j} |F_i - F_j| / \sqrt{\sigma_{F_i}^2 + \sigma_{F_j}^2}$$

<sup>c</sup>  $R = F_{\text{max}}/F_{\text{min}}$ . For sources with no detected flux in at least one of the observations a lower limit with  $3\sigma$  Gaussian confidence is given.

$$^d S_{\text{HR1}} = \max_{i,j} |\text{HR1}_i - \text{HR1}_j| / \sqrt{\sigma_{\text{HR1},i}^2 + \sigma_{\text{HR1},j}^2}$$

$$^e S_{\text{HR2}} = \max_{i,j} |\text{HR2}_i - \text{HR2}_j| / \sqrt{\sigma_{\text{HR2},i}^2 + \sigma_{\text{HR2},j}^2}$$

<sup>f</sup> Short-term flux variability is denoted by “s,” long-term flux variability by “l,” and spectral variability by “sp.”

TABLE 13  
*Chandra* SPECTRAL PROPERTIES FOR NGC 6946 SOURCES

No.	Source Designation CXOU J	Hardness Ratios					
		Obs. ID 1043		Obs. ID 4404		Obs. ID 4631	
		HR1 <sup>a</sup>	HR2 <sup>b</sup>	HR1	HR2	HR1	HR2
1	203419.0+601007	0.09 ± 0.10	-0.07 ± 0.10	-0.12 ± 0.37	0.10 ± 0.35	...	...
2	203421.4+601017	0.04 ± 0.08	0.85 ± 0.25	-0.02 ± 0.09	0.92 ± 0.26	...	...
3	203423.4+601039	...	...	0.20 ± 0.16	-0.07 ± 0.17	...	...
4	203424.7+601038	0.09 ± 0.05	0.84 ± 0.19	0.04 ± 0.09	1.25 ± 0.54	...	...
5	203425.0+600906	0.03 ± 0.05	0.15 ± 0.06	0.2 ± 1.0	1.6 ± 3.0	...	...
6	203426.1+600909	0.05 ± 0.02	0.06 ± 0.03	0.08 ± 0.05	-0.03 ± 0.05	...	...
7	203426.2+600914	-1.10 ± 0.25	0.00 ± 0.03	-1.25 ± 0.55	-0.01 ± 0.09	...	...
8	203429.1+601051	0.13 ± 0.15	0.01 ± 0.17	0.03 ± 0.13	0.22 ± 0.17	...	...
9	203431.5+600638	0.04 ± 0.15	0.76 ± 0.39	0.6 ± 1.5	0.2 ± 1.6	...	...
10	203431.5+601056	0.42 ± 0.84	0.7 ± 1.5	0.40 ± 0.78	0.7 ± 1.4	...	...
11	203432.0+601207	0.41 ± 0.29	-0.33 ± 0.29	-0.22 ± 0.32	0.17 ± 0.31	...	...
12	203432.4+600821	0.09 ± 0.08	0.39 ± 0.15	...	...	...	...
13	203434.4+601032	-0.23 ± 0.09	-0.15 ± 0.06	-0.05 ± 0.11	-0.18 ± 0.09	...	...
14	203435.3+600742	-0.80 ± 0.38	-0.11 ± 0.11	-0.72 ± 0.41	-0.17 ± 0.14	...	...
15	203436.1+600839	-0.52 ± 0.18	-0.12 ± 0.08	-0.71 ± 0.33	-0.09 ± 0.12	...	...
16	203436.4+600558	0.17 ± 0.08	0.67 ± 0.24	0.21 ± 0.09	0.54 ± 0.23	...	...
17	203436.5+600930	-0.27 ± 0.03	-0.17 ± 0.02	-0.24 ± 0.04	-0.22 ± 0.02	...	...
18	203437.2+600954	-0.02 ± 0.12	1.04 ± 0.44	0.28 ± 0.24	0.41 ± 0.44	...	...
19	203437.2+601019	-0.03 ± 0.27	-0.14 ± 0.24	0.52 ± 0.43	-0.32 ± 0.46	...	...
20	203437.9+600434	0.13 ± 0.11	-0.04 ± 0.11	0.04 ± 0.15	0.20 ± 0.13	0.24 ± 0.16	0.18 ± 0.16
21	203439.8+600822	0.12 ± 0.06	0.65 ± 0.18	0.07 ± 0.15	1.02 ± 0.58	0.35 ± 0.39	0.72 ± 0.72
22	203440.5+600946	0.11 ± 0.19	1.01 ± 0.70	0.09 ± 0.75	1.3 ± 2.2	-0.33 ± 0.60	0.60 ± 0.63
23	203441.3+600846	0.07 ± 0.25	-0.03 ± 0.26	-0.50 ± 0.69	-0.26 ± 0.37	-0.02 ± 0.35	-0.09 ± 0.27
24	203442.0+600529	-0.03 ± 0.22	0.10 ± 0.24	-0.33 ± 0.63	-0.43 ± 0.29	-0.6 ± 1.1	0.05 ± 0.67
25	203443.1+600652	0.21 ± 0.17	0.29 ± 0.28	0.23 ± 0.56	0.6 ± 1.1	0.32 ± 0.47	0.46 ± 0.74
26	203444.2+600719	0.14 ± 0.86	1.6 ± 2.9	0.09 ± 0.03	0.78 ± 0.12	0.05 ± 0.16	0.39 ± 0.23
27	203445.9+601049	-0.69 ± 0.27	-0.10 ± 0.10	-0.88 ± 0.51	-0.11 ± 0.15	-1.08 ± 0.92	0.27 ± 0.45
28	203446.3+601328	0.24 ± 0.09	0.25 ± 0.14	0.22 ± 0.13	0.34 ± 0.24	0.29 ± 0.14	0.38 ± 0.22
29	203447.1+600850	0.07 ± 0.13	0.20 ± 0.18	...	...	...	...
30	203447.5+601003	-0.25 ± 0.18	-0.19 ± 0.12	0.32 ± 0.23	-0.39 ± 0.22	-0.46 ± 0.32	-0.25 ± 0.15
31	203447.6+600932	-0.38 ± 0.34	-0.26 ± 0.18	0.02 ± 0.08	-0.10 ± 0.07	-0.19 ± 0.62	0.45 ± 0.66
32	203448.4+600811	0.12 ± 0.05	0.05 ± 0.06	0.21 ± 0.07	0.02 ± 0.09	0.10 ± 0.06	0.10 ± 0.08
33	203448.6+600941	0.25 ± 0.13	0.35 ± 0.23	0.32 ± 0.24	0.31 ± 0.40	-0.4 ± 2.0	-0.8 ± 1.6
34	203448.8+600554	-0.59 ± 0.07	-0.12 ± 0.02	-0.50 ± 0.15	-0.20 ± 0.06	-0.72 ± 0.15	-0.14 ± 0.04
35	203449.0+601217	0.05 ± 0.04	0.11 ± 0.05	0.04 ± 0.06	0.03 ± 0.07	0.10 ± 0.08	-0.06 ± 0.08
36	203449.4+601342	-0.09 ± 0.17	0.36 ± 0.22	0.26 ± 0.30	0.05 ± 0.36	0.35 ± 0.65	-0.05 ± 0.59
37	203449.7+601011	0.18 ± 0.16	0.12 ± 0.21	0.38 ± 0.21	0.10 ± 0.30	0.07 ± 0.23	0.67 ± 0.41
38	203449.7+600806	-0.40 ± 0.31	-0.04 ± 0.20	-0.50 ± 0.68	-0.25 ± 0.36	-0.8 ± 1.6	-0.39 ± 0.80
39	203449.7+601020	0.16 ± 0.17	-0.02 ± 0.20	0.55 ± 0.40	-0.34 ± 0.41	0.40 ± 0.24	0.71 ± 0.49
40	203450.0+600924	0.40 ± 0.14	0.03 ± 0.18	0.40 ± 0.17	0.05 ± 0.23	0.13 ± 0.28	0.45 ± 0.40
41	203450.4+601016	0.07 ± 0.18	0.16 ± 0.23	0.07 ± 0.33	-0.06 ± 0.32	0.01 ± 0.37	0.57 ± 0.53
42	203450.4+600724	...	...	0.09 ± 0.08	0.26 ± 0.13	0.11 ± 0.09	0.29 ± 0.13
43	203450.7+600747	-0.21 ± 0.29	-0.32 ± 0.18	-0.32 ± 0.55	-0.30 ± 0.33	-0.10 ± 0.42	-0.22 ± 0.31
44	203450.7+601207	0.27 ± 0.19	0.35 ± 0.31	0.05 ± 0.30	0.04 ± 0.33	0.25 ± 0.28	0.47 ± 0.46
45	203450.9+601020	-0.59 ± 0.16	-0.15 ± 0.06	-0.74 ± 0.35	-0.06 ± 0.13	-0.43 ± 0.27	-0.21 ± 0.14
46	203451.5+601248	0.50 ± 0.28	0.07 ± 0.34	0.12 ± 0.23	0.50 ± 0.41	0.24 ± 0.35	0.11 ± 0.39
47	203451.5+600909	-0.48 ± 0.39	-0.16 ± 0.21	-0.20 ± 0.57	-0.38 ± 0.39	...	...
48	203453.3+601055	-0.35 ± 0.28	-0.32 ± 0.16	-0.43 ± 0.36	-0.14 ± 0.20	-0.75 ± 0.48	-0.28 ± 0.18
49	203453.4+600719	0.04 ± 0.20	0.79 ± 0.50	0.12 ± 0.06	0.71 ± 0.18	0.01 ± 0.92	-0.52 ± 0.78
50	203453.7+600910	0.04 ± 0.18	0.22 ± 0.22	0.02 ± 0.23	0.27 ± 0.30	0.03 ± 0.27	0.11 ± 0.27
51	203455.6+600930	0.61 ± 0.37	-0.28 ± 0.38	0.40 ± 0.23	0.01 ± 0.30	0.49 ± 0.28	-0.16 ± 0.31
52	203456.5+600834	0.12 ± 0.03	0.28 ± 0.05	0.17 ± 0.05	0.22 ± 0.08	0.22 ± 0.05	0.21 ± 0.08
53	203456.5+600819	-0.34 ± 0.23	-0.28 ± 0.12	-0.41 ± 0.29	-0.26 ± 0.14	-0.14 ± 0.27	-0.18 ± 0.19
54	203456.8+600532	-0.03 ± 0.12	0.24 ± 0.14	0.08 ± 0.32	0.28 ± 0.32	0.03 ± 0.19	0.07 ± 0.21
55	203456.9+601209	-0.34 ± 0.37	0.09 ± 0.32	-0.83 ± 0.53	0.16 ± 0.27	-0.11 ± 0.40	0.45 ± 0.51
56	203456.9+600826	0.15 ± 0.48	0.48 ± 0.74	-0.11 ± 0.59	-0.39 ± 0.44	-0.03 ± 0.18	0.05 ± 0.18
57	203457.2+600733	-0.75 ± 0.60	-0.21 ± 0.24	-1.06 ± 0.62	0.12 ± 0.22	0.00 ± 0.88	-0.51 ± 0.75
58	203457.7+600948	0.15 ± 0.03	-0.02 ± 0.04	0.23 ± 0.07	-0.10 ± 0.07	0.17 ± 0.07	0.01 ± 0.08
59	203458.4+600934	0.08 ± 0.13	0.04 ± 0.14	0.08 ± 0.18	-0.28 ± 0.16	0.10 ± 0.25	-0.13 ± 0.24
60	203500.1+600908	-0.27 ± 0.02	-0.20 ± 0.01	-0.31 ± 0.03	-0.19 ± 0.02	-0.33 ± 0.05	-0.22 ± 0.02
61	203500.4+600859	0.17 ± 0.31	0.20 ± 0.39	-0.19 ± 0.30	0.74 ± 0.52	0.09 ± 0.20	0.11 ± 0.23
62	203500.6+601250	0.01 ± 0.12	0.11 ± 0.14	-0.13 ± 0.17	-0.03 ± 0.14	-0.09 ± 0.13	0.13 ± 0.13
63	203500.7+601130	-0.17 ± 0.01	-0.06 ± 0.01	-0.15 ± 0.01	-0.05 ± 0.01	-0.20 ± 0.02	-0.08 ± 0.01
64	203500.9+601010	0.07 ± 0.03	0.20 ± 0.04	0.09 ± 0.05	0.14 ± 0.06	0.06 ± 0.04	0.12 ± 0.05
65	203501.1+600923	-0.55 ± 0.63	-0.34 ± 0.34	-0.16 ± 0.41	-0.15 ± 0.31	0.02 ± 0.96	-0.57 ± 0.86
66	203501.9+601003	0.03 ± 0.05	0.21 ± 0.07	0.04 ± 0.09	0.16 ± 0.11	0.07 ± 0.08	0.26 ± 0.11
67	203504.6+601117	0.14 ± 0.11	-0.36 ± 0.09	-0.15 ± 0.17	-0.31 ± 0.11	-0.14 ± 0.28	-0.43 ± 0.19
68	203504.6+600918	-0.50 ± 0.31	-0.11 ± 0.17	-0.50 ± 0.44	-0.24 ± 0.20	-0.97 ± 0.96	-0.19 ± 0.33
69	203505.3+600623	0.11 ± 0.07	0.27 ± 0.10	0.21 ± 0.14	0.13 ± 0.15	0.21 ± 0.10	0.01 ± 0.12
70	203505.5+600742	-0.03 ± 0.35	0.31 ± 0.45	0.40 ± 0.63	0.00 ± 0.75	-0.29 ± 0.37	0.39 ± 0.39
71	203506.5+601040	0.34 ± 0.14	0.16 ± 0.19	0.34 ± 0.20	-0.06 ± 0.23	0.06 ± 0.24	0.18 ± 0.28
72	203508.1+601113	0.15 ± 0.20	-0.27 ± 0.19	-0.38 ± 0.27	-0.22 ± 0.14	-0.12 ± 0.32	-0.07 ± 0.26



TABLE 13 — *Continued*

No.	Source Designation CXOU J	Hardness Ratios					
		Obs. ID 1043		Obs. ID 4404		Obs. ID 4631	
		HR1 <sup>a</sup>	HR2 <sup>b</sup>	HR1	HR2	HR1	HR2
73	203510.1+601000	-0.16 ± 0.27	0.06 ± 0.25	0.43 ± 0.47	0.11 ± 0.59	0.34 ± 0.34	0.44 ± 0.58
74	203510.9+600856	-0.62 ± 0.42	-0.29 ± 0.18	-0.56 ± 0.55	-0.26 ± 0.26	0.38 ± 0.40	-0.53 ± 0.37
75	203512.5+600837	-0.07 ± 0.49	0.36 ± 0.59	-0.32 ± 0.79	-0.37 ± 0.52	-0.40 ± 0.62	0.35 ± 0.57
76	203512.7+600731	0.10 ± 0.05	0.08 ± 0.06	0.02 ± 0.14	0.13 ± 0.12	0.10 ± 0.08	0.10 ± 0.09
77	203513.1+600907	0.63 ± 0.45	0.08 ± 0.44	0.01 ± 0.18	0.83 ± 0.45	0.28 ± 0.40	0.51 ± 0.71
78	203513.6+600522	...	...	0.09 ± 0.23	0.17 ± 0.22	0.29 ± 0.21	-0.07 ± 0.24
79	203516.2+601046	-0.18 ± 0.11	0.52 ± 0.16	-0.12 ± 0.07	0.14 ± 0.07	0.02 ± 0.08	0.09 ± 0.09
80	203517.3+600813	0.18 ± 0.32	0.18 ± 0.41	-0.8 ± 1.0	0.31 ± 0.51	0.30 ± 0.27	0.29 ± 0.44
81	203518.7+601056	0.26 ± 0.03	0.08 ± 0.04	0.25 ± 0.07	-0.01 ± 0.07	0.28 ± 0.05	0.12 ± 0.08
82	203520.0+600933	-0.50 ± 0.28	0.13 ± 0.19	-0.3 ± 1.1	0.13 ± 0.90	-0.74 ± 0.53	-0.20 ± 0.19
83	203521.1+600951	-0.16 ± 0.28	-0.03 ± 0.23	-0.34 ± 0.54	-0.38 ± 0.29	-0.40 ± 0.36	-0.19 ± 0.20
84	203525.3+600717	...	...	-1.0 ± 2.9	-0.6 ± 1.2	0.07 ± 0.05	0.18 ± 0.06
85	203525.5+600958	-0.22 ± 0.11	-0.11 ± 0.08	-0.21 ± 0.30	-0.26 ± 0.17	-0.03 ± 0.16	-0.22 ± 0.12
86	203527.8+600920	0.05 ± 0.12	0.09 ± 0.14	0.02 ± 0.31	0.14 ± 0.29	0.19 ± 0.18	0.09 ± 0.22
87	203528.6+600605	...	...	0.66 ± 0.66	-0.48 ± 0.55	0.31 ± 0.32	0.20 ± 0.34
88	203530.1+600623	...	...	-0.50 ± 0.32	-0.35 ± 0.13	-0.32 ± 0.10	-0.24 ± 0.07
89	203530.6+600737	...	...	-2.3 ± 1.7	-0.14 ± 0.23	-0.88 ± 0.43	-0.05 ± 0.14
90	203532.2+601018	0.11 ± 0.20	0.37 ± 0.22	...	...	0.36 ± 0.15	-0.10 ± 0.17

<sup>a</sup> Soft color: HR1 = (M - S)/T.<sup>b</sup> Hard color: HR2 = (H - M)/T.TABLE 14  
*Chandra* SPECTRAL PROPERTIES FOR NGC 6946 SOURCES

No.	Source Designation CXOU J	Hardness Ratios					
		Obs. ID 4632		Obs. ID 4633		Combined <sup>c</sup>	
		HR1 <sup>a</sup>	HR2 <sup>b</sup>	HR1	HR2	HR1	HR2
1	203419.0+601007	...	...	0.6 ± 1.4	-0.63 ± 0.82	0.08 ± 0.10	-0.08 ± 0.10
2	203421.4+601017	...	...	1.0 ± 1.8	0.92 ± 1.65	0.02 ± 0.05	0.88 ± 0.17
3	203423.4+601039	...	...	-0.27 ± 0.68	-0.26 ± 0.33	0.09 ± 0.15	-0.12 ± 0.14
4	203424.7+601038	...	...	0.39 ± 0.38	0.32 ± 0.43	0.11 ± 0.04	0.87 ± 0.17
5	203425.0+600906	...	...	0.20 ± 0.21	0.22 ± 0.26	0.03 ± 0.05	0.16 ± 0.06
6	203426.1+600909	...	...	0.01 ± 0.10	-0.04 ± 0.09	0.05 ± 0.02	0.04 ± 0.02
7	203426.2+600914	...	...	-1.5 ± 1.1	-0.07 ± 0.20	-1.18 ± 0.22	-0.01 ± 0.02
8	203429.1+601051	...	...	...	...	0.08 ± 0.10	0.13 ± 0.12
9	203431.5+600638	...	...	...	...	0.08 ± 0.15	0.71 ± 0.37
10	203431.5+601056	...	...	0.20 ± 0.13	-0.29 ± 0.12	0.23 ± 0.12	-0.21 ± 0.12
11	203432.0+601207	-0.64 ± 0.59	0.78 ± 0.59	...	...	-0.08 ± 0.19	0.06 ± 0.18
12	203432.4+600821	...	...	...	...	0.09 ± 0.10	0.39 ± 0.16
13	203434.4+601032	-0.13 ± 0.19	-0.19 ± 0.13	-0.02 ± 0.10	-0.23 ± 0.08	-0.11 ± 0.05	-0.18 ± 0.04
14	203435.3+600742	...	...	-1.1 ± 1.4	-0.11 ± 0.57	-0.80 ± 0.27	-0.14 ± 0.08
15	203436.1+600839	0.3 ± 1.0	-0.70 ± 0.85	-0.95 ± 0.45	-0.20 ± 0.12	-0.63 ± 0.15	-0.15 ± 0.05
16	203436.4+600558	...	...	...	...	0.19 ± 0.05	0.61 ± 0.16
17	203436.5+600930	-0.12 ± 0.05	-0.19 ± 0.03	-0.39 ± 0.06	-0.16 ± 0.03	-0.26 ± 0.02	-0.19 ± 0.01
18	203437.2+600954	-0.25 ± 0.87	0.8 ± 1.1	-0.1 ± 1.5	2.3 ± 5.0	0.04 ± 0.12	0.88 ± 0.30
19	203437.2+601019	-0.8 ± 1.2	0.9 ± 1.1	0.7 ± 1.4	-1.1 ± 1.8	0.06 ± 0.20	-0.12 ± 0.20
20	203437.9+600434	...	...	...	...	0.12 ± 0.07	0.10 ± 0.07
21	203439.8+600822	0.20 ± 0.34	0.35 ± 0.44	0.39 ± 0.19	0.30 ± 0.30	0.18 ± 0.05	0.60 ± 0.13
22	203440.5+600946	0.15 ± 0.40	0.13 ± 0.41	-0.47 ± 0.52	0.60 ± 0.55	-0.08 ± 0.15	0.62 ± 0.25
23	203441.3+600846	-0.03 ± 0.59	-0.01 ± 0.50	-0.45 ± 0.64	-0.15 ± 0.38	-0.10 ± 0.16	-0.09 ± 0.13
24	203442.0+600529	0.8 ± 1.2	-0.9 ± 1.2	0.41 ± 0.30	0.07 ± 0.37	0.04 ± 0.15	-0.09 ± 0.14
25	203443.1+600652	0.07 ± 0.89	-0.11 ± 0.73	-0.5 ± 2.8	-1.1 ± 3.0	0.19 ± 0.14	0.26 ± 0.21
26	203444.2+600719	0.20 ± 0.19	0.13 ± 0.22	0.16 ± 0.22	-0.11 ± 0.22	0.11 ± 0.04	0.58 ± 0.09
27	203445.9+601049	-1.9 ± 2.3	0.09 ± 0.67	-0.54 ± 0.60	-0.11 ± 0.37	-0.84 ± 0.22	-0.05 ± 0.08
28	203446.3+601328	0.32 ± 0.23	0.17 ± 0.23	-0.11 ± 0.25	0.72 ± 0.29	0.22 ± 0.05	0.35 ± 0.09
29	203447.1+600850	...	...	...	...	0.01 ± 0.17	0.16 ± 0.19
30	203447.5+601003	-0.28 ± 0.29	-0.21 ± 0.18	-0.82 ± 0.44	-0.10 ± 0.16	-0.28 ± 0.11	-0.22 ± 0.06
31	203447.6+600932	-0.31 ± 0.40	0.17 ± 0.33	0.19 ± 0.09	-0.04 ± 0.10	0.03 ± 0.06	-0.06 ± 0.05
32	203448.4+600811	0.08 ± 0.12	-0.03 ± 0.12	0.07 ± 0.06	0.22 ± 0.08	0.12 ± 0.03	0.09 ± 0.03
33	203448.6+600941	...	...	...	...	0.36 ± 0.15	0.27 ± 0.20
34	203448.8+600554	-0.70 ± 0.14	-0.17 ± 0.04	-0.51 ± 0.11	-0.20 ± 0.04	-0.60 ± 0.05	-0.15 ± 0.02
35	203449.0+601217	0.17 ± 0.08	0.13 ± 0.10	0.20 ± 0.06	0.08 ± 0.08	0.09 ± 0.03	0.06 ± 0.03
36	203449.4+601342	0.94 ± 0.74	-0.17 ± 0.56	0.64 ± 0.55	0.60 ± 0.65	0.15 ± 0.12	0.24 ± 0.15
37	203449.7+601011	0.21 ± 0.19	0.58 ± 0.36	-0.02 ± 0.38	0.20 ± 0.39	0.18 ± 0.08	0.33 ± 0.13
38	203449.7+600806	-0.90 ± 0.71	-0.19 ± 0.23	-0.69 ± 0.86	0.09 ± 0.49	-0.58 ± 0.24	-0.11 ± 0.11
39	203449.7+601020	0.25 ± 0.52	-0.18 ± 0.47	-0.09 ± 0.78	0.65 ± 0.97	0.25 ± 0.12	0.14 ± 0.14
40	203450.0+600924	0.10 ± 0.28	0.53 ± 0.41	0.06 ± 0.22	0.36 ± 0.27	0.26 ± 0.08	0.22 ± 0.11
41	203450.4+601016	0.22 ± 0.49	-0.11 ± 0.44	...	...	0.11 ± 0.13	0.22 ± 0.16
42	203450.4+600724	0.19 ± 0.10	0.02 ± 0.12	0.01 ± 0.13	-0.01 ± 0.12	0.11 ± 0.04	0.16 ± 0.06

TABLE 14 — *Continued*

No.	Source Designation CXOU J	Hardness Ratios					
		Obs. ID 4632		Obs. ID 4633		Combined <sup>c</sup>	
		HR1 <sup>a</sup>	HR2 <sup>b</sup>	HR1	HR2	HR1	HR2
43	203450.7+600747	-0.00 ± 0.57	-0.47 ± 0.44	-0.25 ± 0.69	-0.06 ± 0.53	-0.18 ± 0.17	-0.29 ± 0.11
44	203450.7+601207	0.53 ± 0.56	-0.35 ± 0.59	-1.5 ± 4.2	1.5 ± 4.2	0.21 ± 0.12	0.24 ± 0.18
45	203450.9+601020	-0.26 ± 0.28	-0.38 ± 0.16	-0.62 ± 0.37	-0.23 ± 0.14	-0.55 ± 0.11	-0.19 ± 0.04
46	203451.5+601248	0.18 ± 0.29	-0.05 ± 0.30	0.31 ± 0.53	-0.00 ± 0.55	0.28 ± 0.12	0.13 ± 0.15
47	203451.5+600909	-0.12 ± 0.51	-0.30 ± 0.38	-0.22 ± 0.47	0.30 ± 0.45	-0.33 ± 0.22	-0.09 ± 0.14
48	203453.3+601055	0.10 ± 0.46	-0.62 ± 0.41	-0.43 ± 0.52	-0.41 ± 0.28	-0.40 ± 0.16	-0.32 ± 0.08
49	203453.4+600719	0.27 ± 0.20	0.44 ± 0.38	0.18 ± 0.18	0.71 ± 0.47	0.14 ± 0.05	0.65 ± 0.13
50	203453.7+600910	0.02 ± 0.25	0.17 ± 0.27	0.58 ± 0.31	0.06 ± 0.35	0.11 ± 0.09	0.18 ± 0.11
51	203455.6+600930	0.38 ± 0.18	-0.16 ± 0.20	0.03 ± 0.18	0.04 ± 0.19	0.32 ± 0.09	-0.08 ± 0.10
52	203456.5+600834	0.13 ± 0.05	0.21 ± 0.08	0.17 ± 0.04	0.28 ± 0.07	0.15 ± 0.02	0.25 ± 0.03
53	203456.5+600819	-0.58 ± 0.56	-0.24 ± 0.25	-1.00 ± 0.52	-0.10 ± 0.13	-0.44 ± 0.13	-0.22 ± 0.06
54	203456.8+600532	0.17 ± 0.16	0.19 ± 0.22	-0.23 ± 0.19	0.27 ± 0.19	-0.02 ± 0.07	0.21 ± 0.08
55	203456.9+601209	0.07 ± 0.61	0.16 ± 0.65	-0.9 ± 1.1	0.9 ± 1.1	-0.42 ± 0.20	0.28 ± 0.18
56	203456.9+600826	0.17 ± 0.55	-0.15 ± 0.52	0.04 ± 0.20	0.06 ± 0.21	0.03 ± 0.11	0.04 ± 0.11
57	203457.2+600733	...	...	...	...	-0.77 ± 0.36	-0.14 ± 0.13
58	203457.7+600948	0.21 ± 0.07	-0.08 ± 0.08	0.13 ± 0.06	-0.02 ± 0.07	0.17 ± 0.02	-0.04 ± 0.03
59	203458.4+600934	0.03 ± 0.21	-0.12 ± 0.19	0.18 ± 0.25	-0.27 ± 0.22	0.09 ± 0.07	-0.12 ± 0.07
60	203500.1+600908	-0.31 ± 0.05	-0.19 ± 0.02	-0.34 ± 0.05	-0.19 ± 0.03	-0.31 ± 0.01	-0.20 ± 0.01
61	203500.4+600859	0.12 ± 0.23	0.13 ± 0.28	-0.12 ± 0.65	0.49 ± 0.82	0.06 ± 0.10	0.26 ± 0.14
62	203500.6+601250	0.21 ± 0.19	-0.03 ± 0.23	0.12 ± 0.27	0.19 ± 0.35	-0.01 ± 0.06	0.08 ± 0.07
63	203500.7+601130	-0.21 ± 0.02	-0.07 ± 0.01	-0.21 ± 0.02	-0.06 ± 0.01	-0.18 ± 0.01	-0.06 ± 0.00
64	203500.9+601010	0.04 ± 0.05	0.20 ± 0.07	0.06 ± 0.05	0.32 ± 0.08	0.07 ± 0.02	0.19 ± 0.03
65	203501.1+600923	0.9 ± 1.7	-0.9 ± 1.7	-0.35 ± 0.64	-0.36 ± 0.38	-0.23 ± 0.24	-0.34 ± 0.16
66	203501.9+601003	0.11 ± 0.10	-0.02 ± 0.11	0.02 ± 0.08	0.20 ± 0.10	0.05 ± 0.03	0.18 ± 0.04
67	203504.6+601117	-0.11 ± 0.22	-0.36 ± 0.16	0.07 ± 0.18	-0.40 ± 0.14	0.01 ± 0.07	-0.37 ± 0.05
68	203504.6+600918	-0.03 ± 0.51	-0.44 ± 0.40	0.06 ± 0.45	-0.45 ± 0.36	-0.41 ± 0.18	-0.24 ± 0.09
69	203505.3+600623	0.09 ± 0.10	0.19 ± 0.13	0.29 ± 0.10	0.04 ± 0.13	0.16 ± 0.04	0.15 ± 0.05
70	203505.5+600742	-0.01 ± 0.34	0.51 ± 0.52	0.23 ± 0.24	0.52 ± 0.50	0.00 ± 0.13	0.39 ± 0.19
71	203506.5+601040	0.19 ± 0.20	0.18 ± 0.26	0.09 ± 0.12	0.46 ± 0.21	0.21 ± 0.06	0.22 ± 0.09
72	203508.1+601113	0.04 ± 0.32	0.06 ± 0.32	-0.06 ± 0.32	-0.33 ± 0.24	-0.07 ± 0.11	-0.19 ± 0.08
73	203510.1+601000	0.07 ± 0.36	-0.09 ± 0.34	0.01 ± 0.43	0.39 ± 0.57	0.05 ± 0.14	0.14 ± 0.15
74	203510.9+600856	-0.66 ± 0.54	-0.21 ± 0.21	-0.35 ± 0.60	-0.33 ± 0.35	-0.41 ± 0.19	-0.31 ± 0.09
75	203512.5+600837	0.10 ± 0.42	0.09 ± 0.47	-0.02 ± 0.49	0.23 ± 0.56	-0.12 ± 0.20	0.17 ± 0.20
76	203512.7+600731	0.00 ± 0.07	0.17 ± 0.08	-0.06 ± 0.07	0.15 ± 0.08	0.04 ± 0.03	0.12 ± 0.03
77	203513.1+600907	0.32 ± 0.66	0.7 ± 1.2	0.44 ± 0.41	0.00 ± 0.49	0.31 ± 0.13	0.44 ± 0.22
78	203513.6+600522	0.01 ± 0.21	0.19 ± 0.25	0.39 ± 0.37	0.00 ± 0.46	0.16 ± 0.10	0.10 ± 0.12
79	203516.2+601046	-2.2 ± 3.8	-0.27 ± 0.90	0.18 ± 0.27	0.26 ± 0.37	-0.07 ± 0.04	0.20 ± 0.05
80	203517.3+600813	0.06 ± 0.30	0.36 ± 0.44	0.48 ± 0.47	-0.25 ± 0.50	0.14 ± 0.13	0.21 ± 0.18
81	203518.7+601056	0.33 ± 0.05	0.01 ± 0.07	0.30 ± 0.05	-0.04 ± 0.07	0.28 ± 0.02	0.04 ± 0.03
82	203520.0+600933	-1.7 ± 3.1	-0.23 ± 0.94	-0.36 ± 0.83	-0.35 ± 0.51	-0.60 ± 0.23	-0.01 ± 0.12
83	203521.1+600951	-0.33 ± 0.36	-0.20 ± 0.22	-0.36 ± 0.66	-0.35 ± 0.38	-0.29 ± 0.16	-0.18 ± 0.10
84	203525.3+600717	0.04 ± 0.06	0.10 ± 0.07	0.08 ± 0.06	-0.01 ± 0.06	0.04 ± 0.03	0.08 ± 0.03
85	203525.5+600958	-0.11 ± 0.22	-0.32 ± 0.15	-0.29 ± 0.20	-0.24 ± 0.11	-0.18 ± 0.07	-0.20 ± 0.05
86	203527.8+600920	0.08 ± 0.17	0.39 ± 0.27	0.15 ± 0.20	0.09 ± 0.24	0.09 ± 0.07	0.14 ± 0.09
87	203528.6+600605	0.03 ± 0.34	-0.07 ± 0.32	0.60 ± 0.77	-0.61 ± 0.76	0.30 ± 0.18	-0.15 ± 0.19
88	203530.1+600623	-0.43 ± 0.19	-0.19 ± 0.09	-0.43 ± 0.19	-0.26 ± 0.09	-0.40 ± 0.09	-0.25 ± 0.04
89	203530.6+600737	-0.85 ± 0.42	-0.15 ± 0.12	-0.99 ± 0.42	-0.10 ± 0.10	-1.06 ± 0.25	-0.11 ± 0.05
90	203532.2+601018	-0.04 ± 0.17	0.28 ± 0.20	0.13 ± 0.23	-0.12 ± 0.20	0.15 ± 0.08	0.13 ± 0.09

<sup>a</sup> Soft color:  $HR1 = (M - S)/T$ .<sup>b</sup> Hard color:  $HR2 = (H - M)/T$ .<sup>c</sup> Hardness ratios calculated from the co-added exposure.

TABLE 15  
*Chandra* SPECTRAL PROPERTIES FOR NGC 4485/4490 SOURCES

No.	Source Designation CXOU J	Hardness Ratios							
		Obs. ID 1579		Obs. ID 4725		Obs. ID 4726		Combined <sup>c</sup>	
		HR1 <sup>a</sup>	HR2 <sup>b</sup>	HR1	HR2	HR1	HR2	HR1	HR2
1	123025.2+413924	0.13 ± 0.08	0.08 ± 0.11	0.01 ± 0.07	0.35 ± 0.10	0.12 ± 0.06	0.25 ± 0.09	0.08 ± 0.04	0.25 ± 0.06
2	123026.7+413821	...	...	-0.15 ± 0.22	-0.05 ± 0.17	0.22 ± 0.20	-0.04 ± 0.22	0.03 ± 0.13	-0.04 ± 0.13
3	123027.1+413814	0.15 ± 0.10	0.74 ± 0.34	0.09 ± 0.12	0.24 ± 0.16	0.08 ± 0.10	0.52 ± 0.20	0.10 ± 0.06	0.45 ± 0.11
4	123027.6+413941	-0.12 ± 0.69	0.24 ± 0.82	0.36 ± 0.49	-0.31 ± 0.46	-0.05 ± 0.21	0.09 ± 0.21	0.03 ± 0.17	0.02 ± 0.17
5	123028.2+413958	-0.06 ± 0.23	-0.24 ± 0.19	-0.51 ± 0.53	-0.10 ± 0.29	0.49 ± 0.55	0.10 ± 0.65	-0.14 ± 0.19	-0.15 ± 0.14
6	123028.5+413926	0.13 ± 0.16	0.55 ± 0.35	0.33 ± 0.17	0.32 ± 0.29	-0.02 ± 0.20	0.70 ± 0.40	0.16 ± 0.09	0.51 ± 0.18
7	123028.7+413757	-0.20 ± 0.30	-0.15 ± 0.23	-0.07 ± 0.15	0.41 ± 0.22	-0.31 ± 0.11	0.36 ± 0.11	-0.23 ± 0.08	0.33 ± 0.09
8	123029.0+414046	-0.11 ± 0.22	0.09 ± 0.24	-0.07 ± 0.17	0.03 ± 0.16	-0.24 ± 0.25	-0.01 ± 0.19	-0.13 ± 0.11	0.03 ± 0.10
9	123029.4+413927	0.24 ± 0.03	0.44 ± 0.07	0.20 ± 0.02	0.47 ± 0.05	0.20 ± 0.03	0.46 ± 0.06	0.21 ± 0.01	0.46 ± 0.03
10	123029.4+414058	-0.51 ± 0.90	-0.23 ± 0.55	-0.98 ± 0.65	-0.20 ± 0.19	-0.49 ± 0.52	0.40 ± 0.46	-0.72 ± 0.35	0.02 ± 0.17
11	123030.3+413853	0.12 ± 0.05	0.26 ± 0.08	0.07 ± 0.04	0.16 ± 0.05	-0.03 ± 0.10	0.03 ± 0.10	0.07 ± 0.03	0.17 ± 0.04
12	123030.3+414126	...	...	0.10 ± 0.19	0.04 ± 0.20	0.25 ± 0.13	-0.02 ± 0.15	0.20 ± 0.10	0.01 ± 0.12
13	123030.4+414142	0.07 ± 0.02	0.13 ± 0.02	0.02 ± 0.02	0.06 ± 0.02	0.05 ± 0.02	0.11 ± 0.02	0.04 ± 0.01	0.10 ± 0.01
14	123030.7+413911	0.25 ± 0.02	0.31 ± 0.04	0.24 ± 0.01	0.29 ± 0.03	0.23 ± 0.01	0.29 ± 0.03	0.24 ± 0.01	0.29 ± 0.02
15	123031.0+413837	0.21 ± 0.19	0.31 ± 0.33	0.38 ± 0.27	-0.14 ± 0.28	0.24 ± 0.15	0.43 ± 0.27	0.26 ± 0.10	0.24 ± 0.15
16	123031.3+413901	0.17 ± 0.19	0.46 ± 0.37	-0.15 ± 0.35	0.07 ± 0.30	-0.01 ± 0.14	0.17 ± 0.16	0.01 ± 0.10	0.21 ± 0.12
17	123031.6+414140	-2.0 ± 9.5	-0.2 ± 3.4	-0.12 ± 0.05	-0.07 ± 0.04	-0.12 ± 0.03	0.02 ± 0.03	-0.10 ± 0.03	0.00 ± 0.02
18	123032.1+413918	0.16 ± 0.03	0.17 ± 0.04	0.19 ± 0.02	0.22 ± 0.02	0.18 ± 0.01	0.26 ± 0.02	0.18 ± 0.01	0.23 ± 0.02
19	123032.8+413845	-0.19 ± 0.68	-0.33 ± 0.52	0.28 ± 0.40	-0.34 ± 0.35	-0.14 ± 0.28	-0.06 ± 0.22	-0.02 ± 0.19	-0.18 ± 0.15
20	123032.9+414014	0.12 ± 0.31	0.28 ± 0.47	0.08 ± 0.12	0.52 ± 0.22	0.22 ± 0.14	0.32 ± 0.23	0.14 ± 0.08	0.42 ± 0.14
21	123034.1+413859	2 ± 14	-2 ± 12	0.31 ± 0.14	0.41 ± 0.27	0.15 ± 0.16	0.39 ± 0.26	0.24 ± 0.10	0.39 ± 0.18
22	123034.2+413805	0.14 ± 0.13	0.41 ± 0.25	0.06 ± 0.11	0.82 ± 0.32	0.23 ± 0.17	0.67 ± 0.42	0.12 ± 0.07	0.62 ± 0.17
23	123034.3+413850	0.12 ± 0.06	0.02 ± 0.07	0.06 ± 0.08	-0.17 ± 0.07	-0.06 ± 0.06	0.17 ± 0.06	0.03 ± 0.04	0.04 ± 0.04
24	123034.5+413834	-0.79 ± 0.71	-0.11 ± 0.28	-1.28 ± 0.62	0.11 ± 0.16	-1.28 ± 0.60	0.08 ± 0.15	-1.17 ± 0.35	0.06 ± 0.08
25	123035.1+413846	0.25 ± 0.13	0.05 ± 0.17	0.11 ± 0.03	0.07 ± 0.04	0.05 ± 0.03	0.13 ± 0.03	0.09 ± 0.02	0.10 ± 0.02
26	123035.8+413832	0.21 ± 0.25	-0.02 ± 0.29	-0.29 ± 0.21	0.40 ± 0.22	-0.09 ± 0.27	-0.31 ± 0.19	-0.11 ± 0.13	0.08 ± 0.12
27	123036.2+413837	0.19 ± 0.02	0.19 ± 0.04	0.22 ± 0.04	-0.04 ± 0.04	0.21 ± 0.02	0.14 ± 0.02	0.21 ± 0.01	0.13 ± 0.02
28	123037.7+413823	-0.23 ± 0.40	0.54 ± 0.59	0.09 ± 0.24	0.63 ± 0.46	0.13 ± 0.34	-0.12 ± 0.32	0.02 ± 0.16	0.34 ± 0.22
29	123038.2+413831	-0.14 ± 0.31	-0.32 ± 0.22	-0.41 ± 0.31	-0.06 ± 0.18	0.12 ± 0.32	-0.11 ± 0.31	-0.20 ± 0.17	-0.15 ± 0.12
30	123038.4+413831	...	...	...	...	0.25 ± 0.02	0.24 ± 0.03	0.25 ± 0.02	0.25 ± 0.03
31	123038.4+413743	-0.28 ± 0.13	0.05 ± 0.10	-0.30 ± 0.12	0.00 ± 0.08	-0.10 ± 0.12	-0.05 ± 0.10	-0.24 ± 0.07	0.00 ± 0.05
32	123038.8+413810	0.32 ± 0.09	0.11 ± 0.13	0.21 ± 0.06	0.34 ± 0.12	0.21 ± 0.03	0.47 ± 0.08	0.23 ± 0.03	0.38 ± 0.06
33	123040.3+413813	0.11 ± 0.06	0.20 ± 0.09	0.15 ± 0.04	0.26 ± 0.07	0.18 ± 0.04	0.24 ± 0.06	0.15 ± 0.03	0.24 ± 0.04
34	123043.0+413756	0.00 ± 0.25	-0.37 ± 0.20	-0.58 ± 0.43	-0.24 ± 0.18	0.01 ± 0.23	-0.26 ± 0.18	-0.15 ± 0.15	-0.29 ± 0.10
35	123043.1+413818	0.20 ± 0.02	0.22 ± 0.03	0.22 ± 0.02	0.10 ± 0.02	0.21 ± 0.01	0.21 ± 0.02	0.21 ± 0.01	0.18 ± 0.01
36	123045.5+413640	-0.04 ± 0.20	-0.21 ± 0.16	0.19 ± 0.10	0.08 ± 0.12	0.13 ± 0.14	0.02 ± 0.15	0.12 ± 0.07	0.01 ± 0.08
37	123047.7+413807	-0.13 ± 0.27	0.32 ± 0.36	0.10 ± 0.27	0.02 ± 0.27	0.21 ± 0.21	0.20 ± 0.29	0.06 ± 0.13	0.17 ± 0.16
38	123047.7+413727	-0.18 ± 0.15	-0.03 ± 0.12	0.04 ± 0.19	0.07 ± 0.20	0.03 ± 0.21	0.17 ± 0.24	-0.10 ± 0.10	0.04 ± 0.09

<sup>a</sup> Soft color:  $HR1 = (M - S)/T$ .<sup>b</sup> Hard color:  $HR2 = (H - M)/T$ .<sup>c</sup> Hardness ratios calculated from the co-added exposure.